

Fall 12-2015

An Investigation of Cooling Configurations in Gas Turbine Engines Using Jet Impingement

Bhushan Upalkar
Embry-Riddle Aeronautical University

Follow this and additional works at: <https://commons.erau.edu/edt>



Part of the [Aerospace Engineering Commons](#)

Scholarly Commons Citation

Upalkar, Bhushan, "An Investigation of Cooling Configurations in Gas Turbine Engines Using Jet Impingement" (2015). *Doctoral Dissertations and Master's Theses*. 254.
<https://commons.erau.edu/edt/254>

This Thesis - Open Access is brought to you for free and open access by Scholarly Commons. It has been accepted for inclusion in Doctoral Dissertations and Master's Theses by an authorized administrator of Scholarly Commons. For more information, please contact commons@erau.edu.

AN INVESTIGATION OF COOLING CONFIGURATIONS
IN GAS TURBINE ENGINES USING JET IMPINGEMENT

A Thesis

Submitted to the Faculty

of

Embry-Riddle Aeronautical University

by

Bhushan Upalkar

In Partial Fulfillment of the

Requirements for the Degree

of

Master of Science in Aerospace Engineering

December 2015

Embry-Riddle Aeronautical University

Daytona Beach, Florida



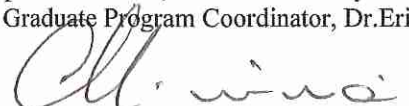



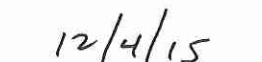
AN INVESTIGATION OF COOLING CONFIGURATIONS
IN GAS TURBINE ENGINES USING JET IMPINGEMENT

by

Bhushan Upalkar

A Thesis prepared under the direction of the candidate's committee chairman, Dr. Mark Ricklick, Department of Aerospace Engineering, and has been approved by the members of the thesis committee. It was submitted to the School of Graduate Studies and Research and was accepted in partial fulfillment of the requirements for the degree of Master of Science in Aerospace Engineering.

THESIS COMMITTEE


Chairman, Dr. Mark Ricklick
Member, Dr. Lakshmanan Narayanaswami
Member, Dr. J. Gordon Leishman
Department Chair, Dr. Anastasios Lyrantzis
or Graduate Program Coordinator, Dr. Eric Perrell
Dean of College of Engineering, Dr. Maj Mirmirani
Associate VP for Academics, Dr. Christopher Grant
Date
Date
Date

ACKNOWLEDGMENTS

I would like to dedicate this work to my family and friends. They have made it possible for me to follow and fuel my interests whatever be the situation. I would also like to thank my committee members for all the timely support and the invaluable guidance they have given me. A special thanks to my advisor, Dr. Mark Ricklick, for being patient with me and guiding me at all times, be it work or life, in general.

I would like to thank my fellow classmates, Yash, Royce, Simon, Sravan, Sanjay and Yogesh for all the help, motivation and discussions that helped shape my outlook towards work and life in all aspects. I am highly indebted to Dr. Sandra Boetcher for guiding me through the basics of CFD. I also appreciate all the help received from Bianca, Chase, Farhaan and many other classmates in various phases of this project. A special thanks to Shristi and Ron for all the support on the experimental side from conducting the tests to attaining results. Their support and cooperation has been immense.

I would like to thank everyone in the Gas Turbine Laboratory (Dr. Attia, Madhur, Chris, Alex, Nicole and Jarrett, Daryl), Mike Potash and Bill Russo for their much needed cooperation throughout the time frame of this project. I would also like to thank the support team at CD-ADAPCO for making the computational side of this project possible. Thanks to Christopher Penny, Chao Zhang and Dr. Ricklick, again, for timely resolving any issues or hurdles in STAR-CCM+.

This study was supported by an internal grant from the university to whom I am highly indebted, and also the Department of Aerospace Engineering for providing me a chance to be a part of one of the most distinguished team of research professionals.

TABLE OF CONTENTS

LIST OF TABLES	v
LIST OF FIGURES	vi
NOMENCLATURE	viii
ABBREVIATIONS	ix
ABSTRACT.....	ix
1. Introduction	1
1.1. Turbine Cooling.....	2
2. Literature Review	7
2.1. Introduction to Jet Impingement	7
2.2. Different Correlations Used in Jet Impingement.....	10
2.3. Investigations in Jet Impingement.....	13
3. Problem Statement and Objective	20
4. Methodology and Data Reduction.....	22
4.1. Experimental Model Setup	22
4.2. Computational Model Setup.....	28
5. Results and Discussion	31
5.1. Grid Independence Study and Channel Validation	31
5.2. Benchmarking of Turbulence Models	33
5.3. Experimental Results.....	44
6. Conclusions	51
7. Scope for Future Work	52
REFERENCES	53

LIST OF TABLES

Table 2.1 Constants used in Florschuetz's correlation	11
Table 5.1 Results of Different Turbulence Models	35

LIST OF FIGURES

Figure 1.1 Brayton Cycle T-S Diagram.....	1
Figure 1.2 Flow Fields seen in Arrays of Jets.....	3
Figure 1.3 Insert Plates Inside Hollow Blades.....	4
Figure 1.4 Vortex Guided Pair for Impingement.....	5
Figure 1.5 Rough Surfaces with Impingement.	5
Figure 1.6 Illustration of an Array of Jet Holes	6
Figure 2.1 Different Flows in Impingement.	7
Figure 2.2 Smoke Visualization of Impinging Jet.	8
Figure 2.3 Potential Core Visualization for Re 6000.....	9
Figure 2.4 Potential Core Visualization for Re 10000.....	9
Figure 2.5 Array of Inline Jets Used.....	12
Figure 2.6 Array of Staggered Jets Used.	12
Figure 2.7 CFD and Experimental Results for Heat Trasnfer $Z/D=2$	15
Figure 2.8 Comparison of Turbulence Models for Jet Impingement Profile.....	16
Figure 2.9 Schematic of Flow through Confined and Free Jets.....	17
Figure 2.10 Tangential Flow on a curved surface.....	18
Figure 3.1 Recent Advances in Turbine Inlet Temperature Increase	20
Figure 4.1a CAD Model of the Experimental Setup.....	22
Figure 4.1b Setup as a Part of the Turbine Blade.	22
Figure 4.2 Image of Blower and Manufacturer's Chart	23
Figure 4.3 Heater Strips used (Inconel-625).....	24
Figure 4.4 Sample TSP Calibration Curve.	25
Figure 4.5a Sample of a Cold TSP Image.....	25
Figure 4.5b Sample of a Hot TSP Image.	25
Figure 4.6 Experimental Setup Used.	26
Figure 4.7 Heat Leak vs. Temperature plot.	27
Figure 4.8 Flowchart of Experimental Setup.....	28
Figure 4.9a Image of Mesh Used.....	29
Figure 4.9b Illustration of Prism Layer.....	30
Figure 5.1 Mesh Independence study for the CFD Model.....	31
Figure 5.2 Images for Butterworth Filter.	32
Figure 5.3 Span Averaged Nu for Experimental Rig.....	33

Figure 5.4 Nu Contour for v^2 -f.....	34
Figure 5.5 Nu Contour for EB k- ϵ	34
Figure 5.6 Span Averaged Nu for different turbulence models.	35
Figure 5.7 Jet to averaged jet mass flux ratio..	36
Figure 5.8 Spatial evolution of velocity at different heights for v^2 -f.....	37
Figure 5.9 Spatial evolution of velocity at different heights for EB k- ϵ	39
Figure 5.10 Target wall Nu contours compared with experiment.	40
Figure 5.11 Channel cross-flow to jet mass flux ratios.	41
Figure 5.12 Nu Contours for two different configurations (5.4.3 and 5.2.6).....	42
Figure 5.13 Different Hole Spacing Configurations Used.....	43
Figure 5.14 Nu Contours from Experimental results, $Re = 20,000$	44
Figure 5.15 Span wise averaged Nu plots, $Re = 20,000$	46
Figure 5.16 Nu Contours from Experimental results, $Re = 15,000$	48
Figure 5.17 Span wise averaged Nu plots, $Re = 15,000$	49

NOMENCLATURE

β	Flow Distribution Parameter
ε	Turbulent Dissipation Rate (Tdr) or Strain Energy
η	Efficiency
ϖ	Strain Energy per unit volume
A, B, C, D, m, n	Indices in Florschuetz's Correlation
C_d	Co-efficient of Discharge
d_j	Jet Diameter (m)
f	Friction Factor
G_c	Channel Cross-Flow mass flux (kg/m ²)
G_j	Jet Mass Flux (kg/m ²)
$G_{j,avg}$	Average Jet Mass Flux (kg/m ²)
h	Heat Transfer Coefficient (W/m ² K)
I	Intensity of the paint
I_r	Reference Image Intensity of the paint
k	Turbulent kinetic energy (Tke)
k_{air}	Thermal Conductivity of Air (W/mK)
k_I	Thermal Conductivity of Inconel (W/mK)
m	Mass flow rate (kg/s)
M	Mach Number
n	Number of Holes
N_C	Number of rows of Impingement Holes
n_x, n_y, n_z	Exponents for Florschuetz's Correlation
Nu	Nusselt Number
Nu_F	Nusselt Number predicted by Florschuetz
P_0	Total Pressure (Pa)
P_s	Static Pressure (Pa)
Pr	Prandtl Number
r/D	Distance in Radial Direction
Re	Reynolds Number
Sc	Schmidt Number
St	Strouhal Number
T	Temperature (°C or K)
T_j	Temperature of the jet fluid (°C or K)
T_w	Temperature of the wall (°C or K)
T_3	Turbine Inlet Temperature (°C or K)
T_4	Turbine Exhaust Temperature (°C or K)
x	Distance in Stream wise direction (m)
$x_n (X/D)$	Stream wise distance in terms of Jet Diameters
Y/D	Span wise Distance in terms of Jet Diameters
Z/D	Channel Height in terms of Jet Diameters

ABBREVIATIONS

BR	Blowing Ratio
CAD	Computer Aided Design
CCD	Charge Coupled Device
CFD	Computational Fluid Dynamics
DB	Dittus-Boelter
DNS	Direct Numerical Solution
EB	Elliptic Blending
LED	Light Emitting Diodes
LES	Large Eddy Simulation
PSP	Pressure Sensitive Paint
RANS	Reynolds Averaged Navier Stokes
STAR-CCM+	Simulation of Turbulence in Arbitrary Regions-Computational Continuum Modeling
TSP	Temperature Sensitive Paint

ABSTRACT

A numerical investigation for predicting the heat transfer effects of turbulence was conducted by making a scaled-up model of a section in a jet impingement channel. Different turbulence models were run and the results were compared to experimental data. Experimental comparisons were made for impingement channels between a baseline case, which is a rectangular array of jets of 20 rows and 3 jets per row, and different hole spacing configurations. The heat transfer was measured using Temperature Sensitive Paint. The turbulence model v^2 -f gave the most accurate prediction with an error of about 17% with the EB k- ϵ , with an error of about 22%, being the second most accurate. The configuration B gave comparatively better results among the different configurations, but was still about 20% lower than the baseline case, which appeared to have the highest cooling.

1. Introduction

Gas turbine engines power a majority of the aircraft manufactured. Their high power-to-weight ratio and less number of moving parts, compared to reciprocating engines, has had the attention of aircraft designers since their proficient use started about the time of the World War II. They fulfill about 30% of the whole United States' electricity needs (Electric Power Monthly, June 2015). With the ever rising cost of the materials involved, including fuel, utilizing the maximum possible efficiency of the engine became of utmost importance.

The Brayton cycle (Fig. 1.1), governs the gas turbine engine, which consists of four main processes namely, compression, combustion, expansion and exhaust. A compressor breathes in ambient air, pressurizes it and supplies it to the combustor. The fuel-air mixture is ignited here and the combusted gas is used to rotate the turbine to extract power. The isentropic efficiency for the turbine section is based on the turbine inlet temperature (T_3) and the exhaust temperature (T_4) as

$$\eta = 1 - T_{4s}/T_3 \quad (1)$$

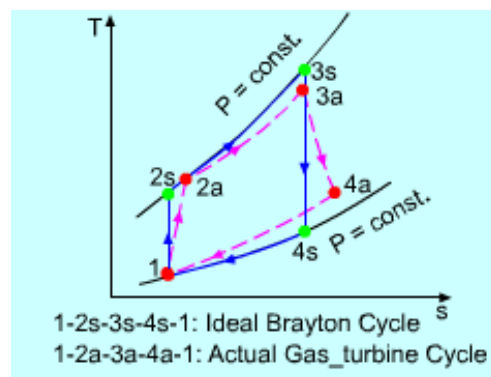


Fig 1.1 T-S Diagram for Brayton Cycle [Efficiency of Gas Turbine, Frompo.com]

T_{4a} - actual temperature after entropy generation, T_4 - after ideal isentropic expansion.

As efficiency increases with increase in T_3 , this value is desired to be as high as possible within safe operating limits of the blade material. Recent advances in material selection with nickel based super alloys and thermal barrier coatings have allowed the T_3 to rise up to 1100°C . But with the technology being populated by the ever increasing market competition, higher inlet temperatures of up to 1400°C were achieved (Gavrieli et al, 2004). Hence, turbine cooling started to be used in tandem with material improvement and has been a major contributor to increasing the efficiency of the engine. Different cooling techniques are employed according to design requirements, like film cooling to cool the outer surface of the blade, impingement cooling for internal cooling of the blade and pin fin cooling in the trailing edge.

1.1.Turbine Cooling

As turbine inlet temperatures T_3 of the order of 1400°C are observed and material advances have elevated the T_3 to about 1100° , the gap of about 300°C is filled by gas turbine cooling technologies. The cooling of turbine blades, combustor lining and guide vanes is primarily done by using cool air from the compressor exit.

Jet impingement technique is an internal cooling technique where the coolant impinges on the hot surface (or target), creating stagnation point flow and a consequent wall jet, as seen in Fig. 1.2. The jet may be free, i.e have no boundaries restricting the direction of the resulting flow or may be confined by side walls limiting the spread of the jet.

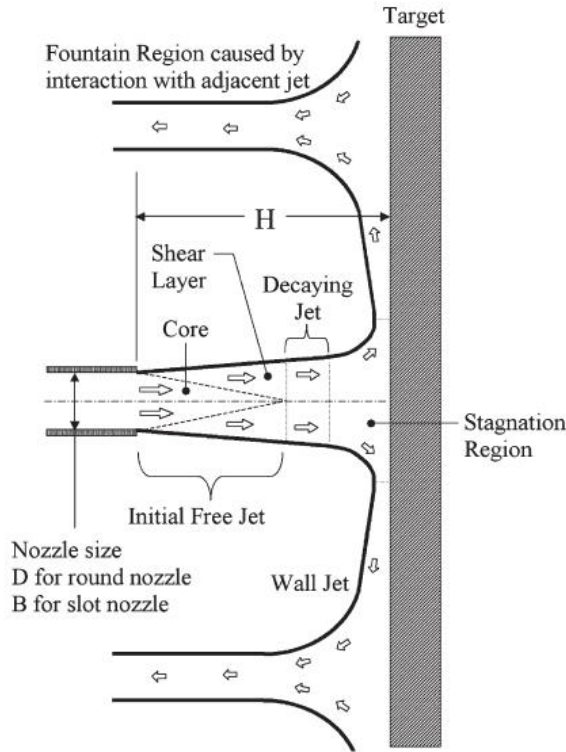


Fig 1.2 Flow regimes observed in impingement arrays for free jets (Zuckerman et al, 2006)

The wall jet interacts with the adjacent jet and forms a fountain which creates flow in the opposite direction of the jet while creating another stagnation region. This increases the heat transfer not only beneath the jet but also between them and hence adds to overall effectiveness. In gas turbine engines, the coolant is the pressurized air from the compressor exit. It may be up to 20% of the total inlet air which ends up as a performance penalty for the compressor. But, in turn, it increases the maximum allowable temperature at turbine inlet and thus increases turbine efficiency. Hence, there is a trade-off to this improved performance.

Jet Impingement channels consist of holes machined on insert plates inside the hollow blades throughout the span, as may be seen in Fig. 1.3 (Girardeau et al, 2013).

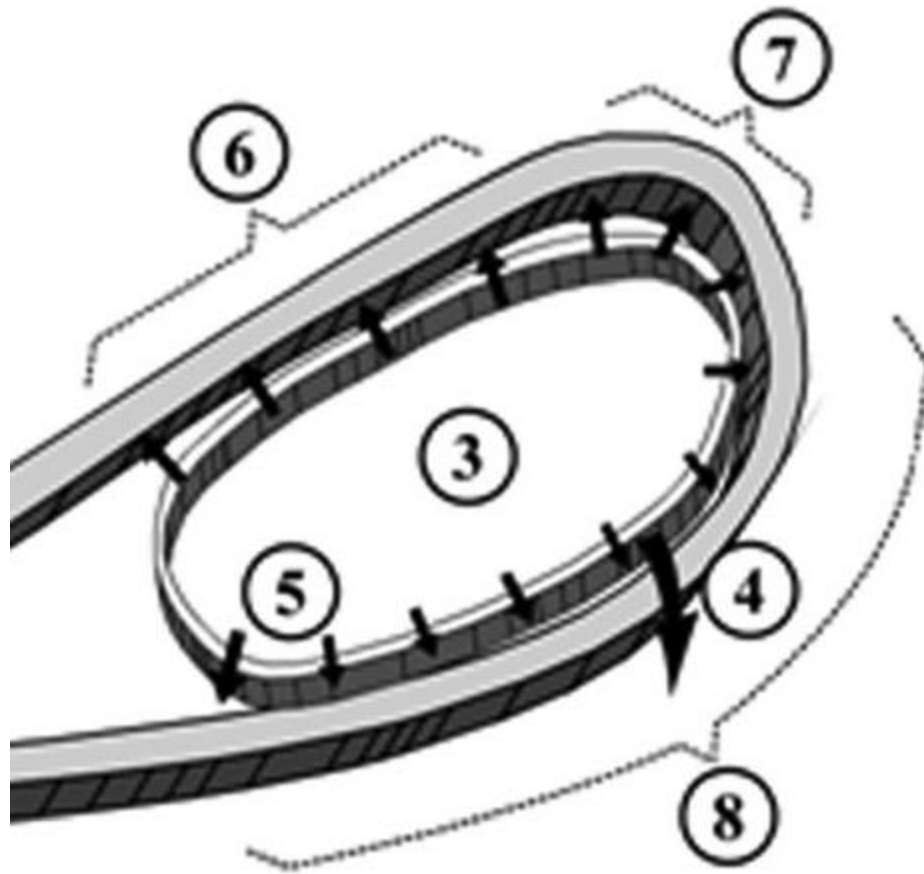


Fig 1.3 Insert plates seen inside the blade with cool air impinging internally on the wall (Girardeau et al, 2013)

The same air may also be used to make a protective layer of coolant directly over the blade surface, which is also known as film cooling, which is beyond the scope of this study.

With multiple effects seen in jet impingement, as discussed above, there is a lot of energy conversion and dissipation which attracts research based interest. Consequently, there is a lot of literature available for experimental and numerical investigations on jet impingement flow and its heat transfer capability, for free and confined jets, coupling

with other heat removal techniques such as film cooling, rib turbulated cooling, pin fin cooling, using vortex generators (as seen in Fig. 1.4) with impingement channels (Wang et al, 2015), varying the spacing between jet holes for different heights (Claretti et al, 2011), staggered and inline jet arrays (Xing et al, 2010), oblique jets (Yan et al, 1997), inclined at an angle to the perpendicular distance from the jet to target plates, curved target surfaces (Choi et al, 1998) and dimpled surfaces, as shown in Fig. 1.5 (Kanokjaruvijit et al, 1997).

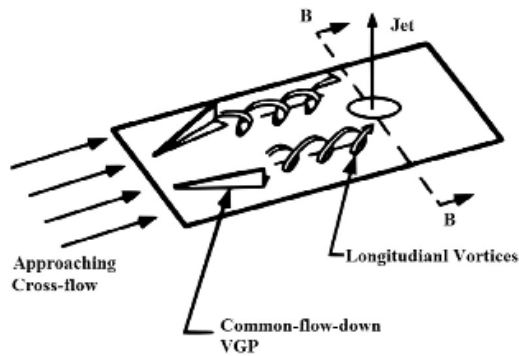
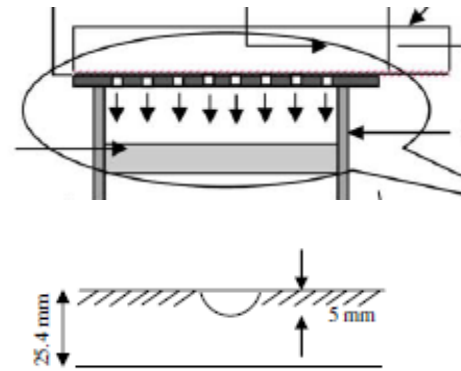


Fig 1.4 Vortex generator pair inducing cross-flow in the direction opposite to the jet flow (Wang et al, 2015)



Rough Surface

Fig 1.5 Impingement on a rough or dimpled surface (Kanokjaruvijit et al, 1997)

This study investigated benchmarking of different turbulence models to determine the best options for impingement channel cooling using an array of jets. Cooling performance was also measured experimentally for different hole spacing configurations in stream wise and span wise directions for inline and staggered arrays at different Re with the goal of using minimum coolant for a given amount of cooling.

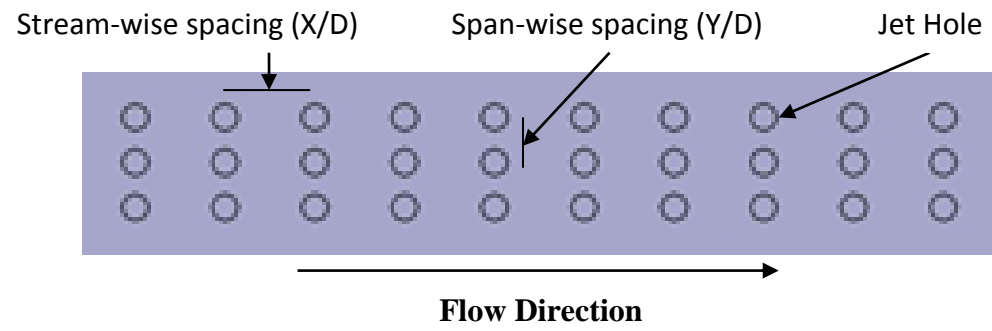


Fig 1.6 A rectangular array of jet holes with stream-wise and span-wise spacing.

2. Literature Review

2.1 Introduction to Jet Impingement

A jet is a rapid stream of fluid being forced out of a small opening. As the flow upstream of a jet enters the opening, it gains a high amount of velocity. With the walls of the jet being stationary, there is a high amount of shear stress at the exit of the jets. For a free circular jet impinging on a surface, there are many flow structures that exist downstream of the exit.

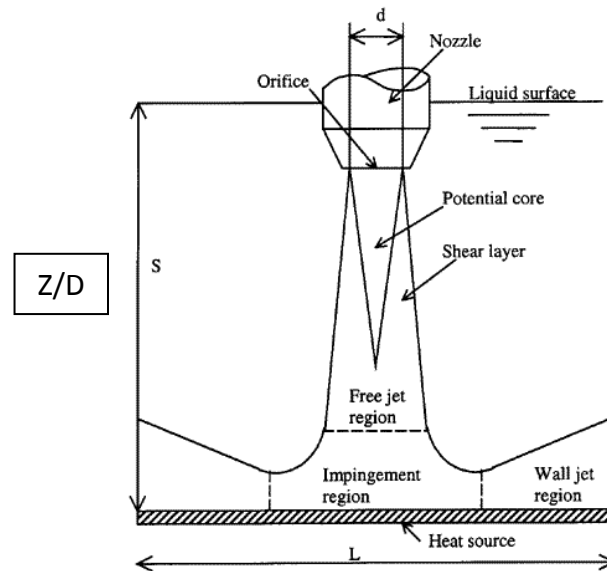


Fig 2.1 Different flow structures observed in jet impingement on a wall (Tadhg et al, 2005)

Defined as the region where the velocity is above or equal to 95% of the jet exit velocity (Tadhg et al, 2005), a potential core is observed in the center region. The shear layer is the region where the core starts breaking and the swirling of the flow begins. This increases the wetted area under the jet. As the incident wall is reached along the path followed by the stream, a stagnation region is observed, directly beneath the jet. In the radially outward direction, a wall jet region which is characterized by a boundary layer

increasing in thickness.

Entrainment of mass, as in Fig. 2.2, was observed by Popiel (Popiel et al, 1991), as a higher velocity created a pressure gradient in the radially inward direction. This caused air from the free stream to flow into the wetted area of the jet. As momentum transport may be linked directly to heat transfer, understanding the flow would better help getting the desired cooling or heat removal.

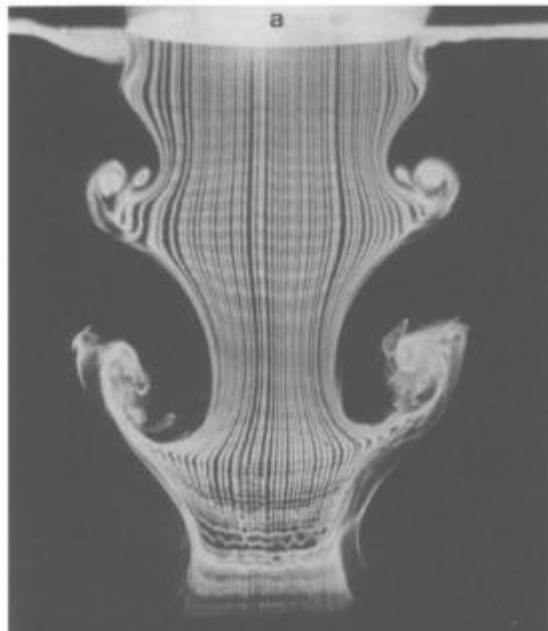


Fig 2.2 Popiel's Flow Visualization showing higher velocity in the center and resulting vorticity and entrainment downstream (Popiel, 1991).

Cornaro (Cornaro et al, 1999) studied visualization of flow in impinging jets for different Re . For a Re of 6000 (Fig. 2.3) the core of the impingement was found at a distance of 4 jet diameters, while that for a Re of 10,000 (Fig. 2.4) was found to break at a distance of 2 jet diameters. This showed that for a longer effective transport of jet momentum from the jet, the Re need not be too high, rather just enough to sustain the impingement core as far as possible. The forming and shedding of vortex structures was

observed, hinting radial oscillations at the end of the core region. This pointed to the flow being unsteady in this region. At lower jet-to-target heights ($Z/D \leq 4$), the vortex structures weren't formed as the potential core did not extend that long to lose energy to the shear layer. This result is significant in the way that for an optimum height, the oscillations in the potential core could be used to spread the stagnation region out consequently increasing the wetted area and the cooling in the stagnation region.

Potential Core breaks at 4 jet diameters

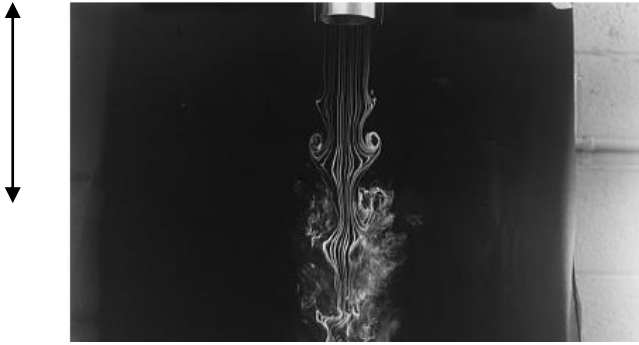


Fig 2.3 Flow visualization for a jet at $Re=6000$ (Cornaro et al, 1999)

Potential Core breaks at 2 jet diameters



Fig 2.4 Flow visualization for a jet at $Re=10000$ (Cornaro et al, 1999)

While other studies with different hole configurations by Metzger et. al (Metzger et al, 1979) found that an inline array performed better than a staggered array of jets, Van Treuren (Van Treuren et al, 1996) found that a staggered array of jets gave a better heat transfer. Son et al (Son et al, 2000) also studied various configurations of staggered and inline arrays at higher average Re , concluding that the average heat transfer came out to be the same. These were run at different Re ranges and hence, in the current work, the local and average heat transfer performance for staggered and inline arrays would be observed to find the one with the highest cooling effectiveness for a given Re and channel configuration.

2.2 Different Correlations in Jet Impingement

The momentum of the jet is transferred normally (or at an angle) to the wall and then, laterally outward. For an array of jets, the wall jets are seen interacting causing a fountain, mentioned earlier, leading to reversed flow and a local heat transfer maximum. As impingement cooling varies with radial and jet-to-target distance, a balance is desired between average and local cooling to reduce thermal stresses. In an attempt to study the effect of a single as well as an array of jets, Martin (Martin, 1977) conducted a wide range of studies on jet impingement heat and mass transfer characteristics for a single jet and array of round and rectangular jets. Mass and heat transfer, in terms of the Sh , Sc , Nu and Pr were related as follows:

$$\frac{Sh}{Sc^{0.42}} = \frac{Nu}{Pr^{0.42}} \quad \dots\dots\dots (1)$$

Predictions for heat transfer at the wall jet and the stagnation flow regions were obtained by Martin as a correlation with the Re and Pr . They were found to be more accurate in the wall jet region than the stagnation region. This was attributed to high turbulence levels at the nozzle exit and the area directly beneath, but this did not change the integral heat transfer coefficients predicted, which were relatively accurate. The correlation for an array of nozzles was empirically obtained in terms of the effective nozzle area, f_a , given as a ratio of jet nozzle area (A) and the effective area of the lines joining the centers of the nozzles and the height Z/D . This relation held good for a limiting value of Z/D .

Florschuetz et al (Florschuetz et al, 1981) studied the heat transfer due to impingement arrays with the goal of establishing empirical correlations for Nu with respect to geometric parameters of the test section. The correlation for the stagnation

point Nu as a function of channel configuration (X, Y and Z/D), flow conditions (Re) and transport-to-thermal diffusivity properties (Pr) was as follows:

$$Nu = A.Re_j^m (1 - B \left[\left(\frac{Z}{D} \right) * \left(\frac{G_c}{G_j} \right)^n \right] * Pr^{1/3} \quad \dots\dots\dots (2)$$

where, A, m, B and n are geometric parameters for inline and staggered constructs calculated as shown:

$$A, m, B, n = C * \left(\frac{X}{D} \right)^{n_x} * \left(\frac{Y}{D} \right)^{n_y} * \left(\frac{Z}{D} \right)^{n_z} \quad \dots\dots\dots (3)$$

For the first row where $\frac{G_c}{G_j} = 0$, the following correlation was used

$$Nu = 0.363 * (X/D)^{n_x} * (Y/D)^{n_y} * (Z/D)^{n_z} \quad \dots\dots\dots (4)$$

The values for the constants n_x , n_y , n_z and C are different for inline and staggered configurations were as follows.

Table 2.1 Constants used in Florschuetz's (Florschuetz, 1981) correlation

	Inline Pattern				Staggered Pattern			
	C	n_x	n_y	n_z	C	n_x	n_y	n_z
A	1.18	-0.944	-0.642	0.169	1.87	-0.771	-0.999	-0.257
m	0.612	0.059	0.032	-0.022	0.571	0.028	0.092	0.039
B	0.437	-0.095	-0.219	0.275	1.03	-0.243	-0.307	0.059
n	0.092	-0.005	0.599	1.04	0.442	0.098	-0.003	0.304

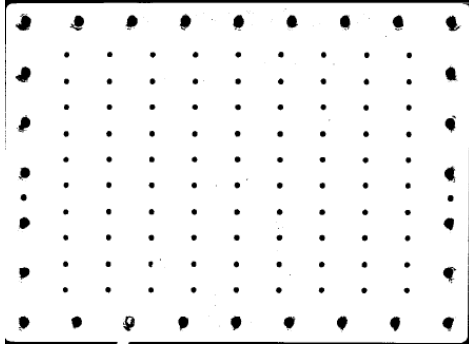


Fig 2.5 Inline array configuration used by Florschuetz (Florschuetz, 1981)

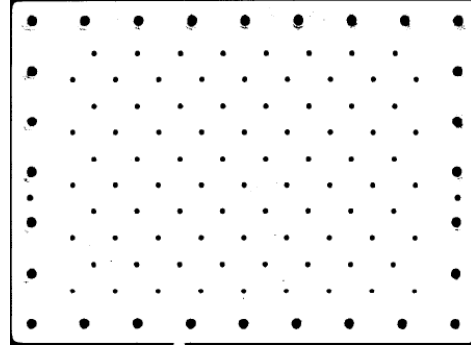


Fig 2.6 Staggered array configuration used by Florschuetz (Florschuetz, 1981)

Also, proposed by Florschuetz et al were 1-dimensional mass flux models for G_j (jet mass flux) and G_c (channel cross-flow mass flux). Pressure ratio profiles (static-to-total pressure) were obtained along the setup for different Re and it was observed that the flow choked (was independent of the downstream pressure) for a Re of around 52000. The choking was observed in the downstream half of the section and only for smaller hole sizes. This led to calculating a coefficient of discharge (C_d) for a range of Re between 2500 and 500000. Different plots gave an average value of the C_d as 0.8 over the given range. A force and mass balance, assuming a constant mass flow model, in lieu of a discrete jet array, was used with boundary conditions. The jet mass flow model obtained was as follows:

$$\frac{G_j}{G_{javg}} = \beta * N_c * \cosh\left(\beta \left(\frac{x}{x_n}\right)\right) / \sinh(\beta * N_c) \quad \dots\dots\dots (5)$$

And the cross-flow model by:

$$\frac{G_c}{G_j} = \frac{1}{\sqrt{2} * C_d} * \sinh\left(\beta \left(\frac{x}{x_n} - \frac{1}{2}\right)\right) / \cosh\left(\beta * \frac{x}{x_n}\right) \quad \dots\dots\dots (6)$$

where,

$$\beta = \frac{\sqrt{2} * C_{d*} \pi / 4}{(\frac{Y}{D} * \frac{Z}{D})} \dots\dots\dots (7)$$

This model fit 95% of all the data points in the 12% fit line with a standard deviation of 5.6%. The larger deviations occurred at lower jet-to-heights ($Z/D = 1$). Hence, this model is used to compare the experimental data acquired herein.

Apart from the Re , the hole spacing and channel height configurations, the Nu has also been related to the Mach number (M) for compressible flow regimes. As determined by Park et al (Park et al, 2007) beyond values of 0.2, the M significantly affects the spatially averaged Nu . The correlation derived was:

$$\frac{Nu}{Nu_F} = 1.1 + 1.2 M^{2.3} \dots\dots\dots (8)$$

where Nu_F was the area averaged Nu predicted by Florschuetz.

Most of these studies were conducted at a fixed hole spacing, for staggered and inline arrays. The current work aims to investigate different cooling configurations to reduce the amount of coolant required to achieve the same cooling as compared to a baseline case.

2.3 Investigations in Jet Impingement

As experimental investigations require a lot of time, money, human effort and troubleshooting, which again amount to increase in time and money, Computational Fluid Dynamics (CFD) has been widely used as an effective tool to replicate the experimental conditions generating results by solving partial differential equations governing the Physics in the experiment with given boundary conditions. It is already being extensively used in industry to simulate different physical situations for automobile design, aircraft performance optimization, electronics and manufacturing. In turbulence cases, CFD

effectively captures the expected trends but the confidence in the values expected is not good enough to stand on its own. The study conducted by El-Gabry (El-Gabry et al, 2005) consisted of experimentally performing jet impingement and running CFD in two different turbulence models, the Yang-Shih and the k- ϵ , at two different jet-to-target heights (1D and 2D) and three different jet inclinations to the target walls (namely, 30°, 60° and 90°). The numerical results of span wise averaged Nu were compared with the experimental ones and there was a shift observed in the downstream direction for stagnation peaks as predicted by the CFD, as seen in Fig. 2.7. The cross-flow shifted the stagnation points, downstream, which wasn't predicted by the CFD. At lower Re , the Yang-Shih model predicted the area averaged Nu on the target wall with reasonable agreement while for higher Re the k- ϵ model predicted more accurately. The Nu at the stagnation point was over predicted which was attributed to higher transfer of the turbulent kinetic energy, Tke (k) to viscous dissipation, by the model than would be present physically. This varied according to how these terms were modeled. Errors of the order of about 25% were found between the numerical predictions and the experimental values. Hence, validation of CFD study with a given set of experiments is required to assert a level of confidence in the former. Also seen was the relative shift of the experimental stagnation peaks from the ones predicted by CFD.

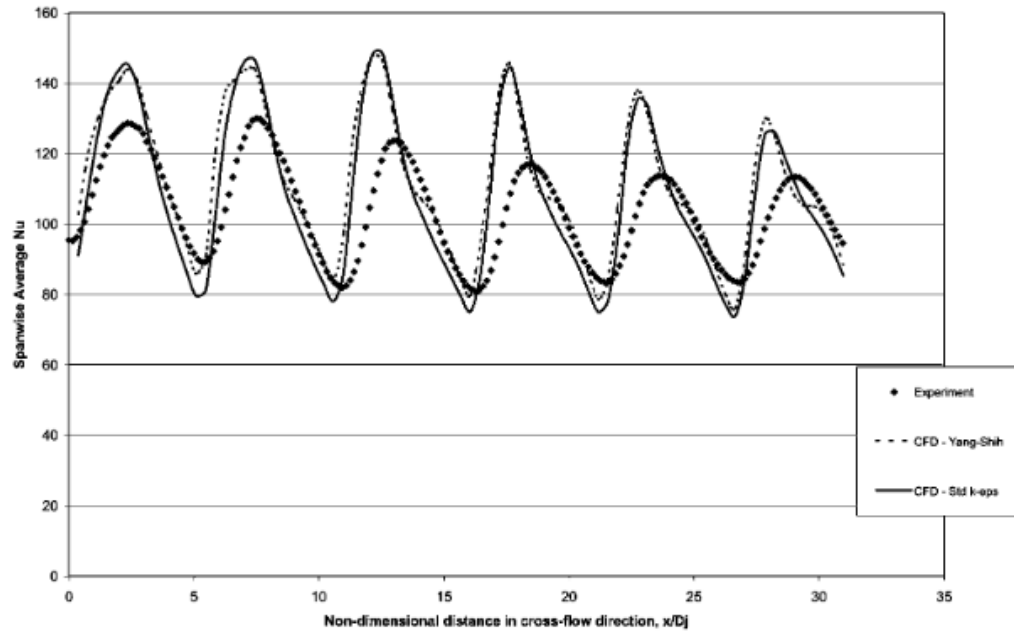


Fig 2.7 Comparison of stagnation peaks for a channel height (Z/D) of 2 jet diameters with an apparent shift in the peaks seen clearly (El-Gabry et al, 2005).

There have been many investigations in jet impingement. Zuckerman (Zuckerman et al, 2006) observed for a radial array of slot jets impinging on a wall, that a secondary peak is observed in the radially outward direction. In the region of the secondary peak, an increase the component of turbulence in the direction normal to the stream was observed. This was believed to influence the heat transfer and the enhancement noted was by an order of magnitude as compared to that observed by a single jet. The resulting flow separation and the aforementioned ‘fountain’ were also observed.

In the same study (Zuckerman et al, 2006), comparisons were made, as seen in Fig. 2.8, among various two-equation models $k-\epsilon$ and the $k-\omega$ turbulence models and their variants, the realizable $k-\epsilon$, Menter’s $k-\omega$ and v^2-f and the six equation Reynolds Stress Model (RSM). The conclusion was that the v^2-f was the only turbulence model that predicted the secondary peak among all the models.

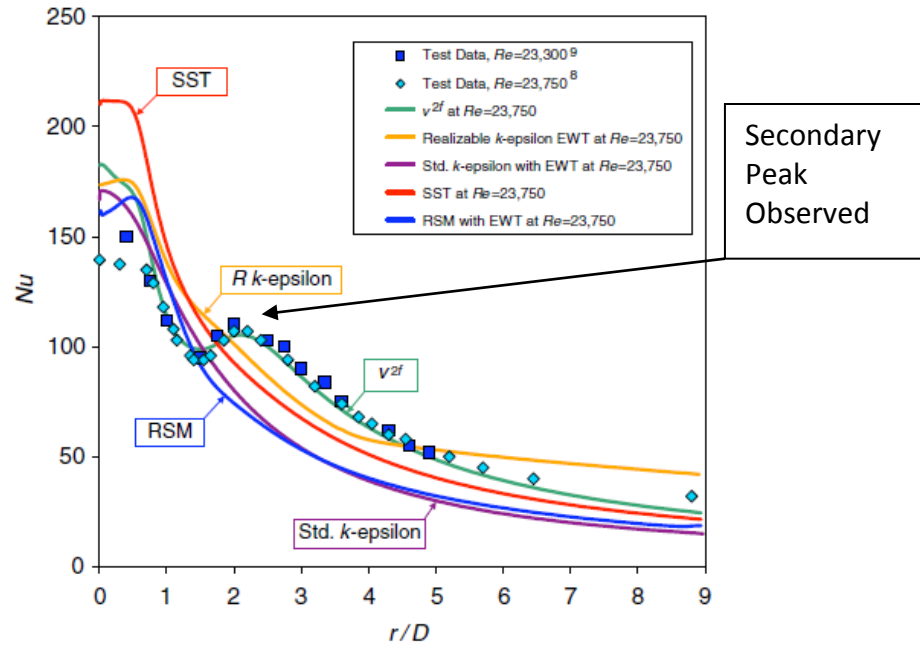


Fig 2.8 Prediction of secondary peak for Jet Impingement (r/D is the non-dimensional radial distance) (Zuckerman et al, 2006).

Durbin (Durbin, 1995) used the v^2 -f model for measuring skin friction and velocity profiles over different kinds of separated flows, namely plane jet diffuser, backward facing step and a triangular cylinder. Good agreement was observed with experimental data and the smooth as well as sharp flow separations were achieved. Vortex shedding for the triangular cylinder case in terms of the St was found to be higher by about 15% from the experimental value of 0.25. This strengthened the case for v^2 -f turbulence model in being robust in predicting the different flow phenomenon taking place in the different locations in jet impingement as discussed earlier.

Hallqvist (Hallqvist et al, 2006) conducted an LES study on an impinging jet with the target surface at a lower temperature than that of the jet. Coherent vortex structures were observed to enhance heat transfer on an average, but as opposed to turbulent flow, these structures reduced the wall heat transfer in the center regions. This was linked to the

sense of rotation of these structures as the counter-rotating secondary vortex observed therein appeared to enhance the heat transfer near the wall. It was found that for small swirl rate heat transfer was enhanced due to increase in turbulent intensity, locally, while for higher swirl rates more spreading of the jet resulted in decreased overall heat transfer.

Behnia et al (Behnia et al, 1998) conducted investigations on confined and unconfined jets in heat transfer. A benchmarking study was done with reference experimental data and it was found that confined jets had a lower heat transfer overall compared to unconfined jets (illustration shown in Fig. 2.9), but the for the stagnation region it remained unchanged for lower channel heights (Z/D).

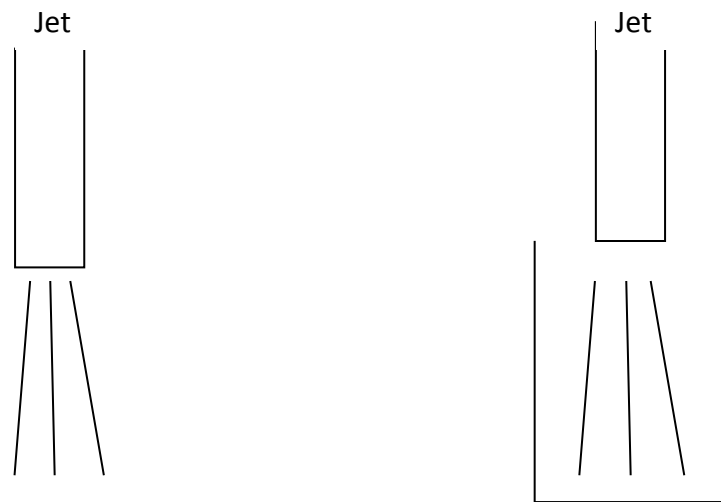


Fig 2.9 Illustration showing flow through a free jet (left) and a confined jet (right)

Mushatat (Mushatat et al, 2007) studied impingement with a slot jet compounded with an initial cross flow with ribs, used for enhancing turbulence, on the target wall. The ribs were usually high aspect ratio pieces, often of a rectangular shape, increasing the contact area for the target wall and hence, the resulting heat transfer. Nu comparisons with existing literature showed that a higher heat transfer was obtained at a higher jet

width to rib thickness ratio and for an increase in jet velocity for a constant cross flow velocity.

Effects of jet nozzle aspect ratio (slot jet width to thickness) and jet inclination angle (with respect to the target wall) were also studied by Liu et al (Liu et al, 2015). As seen in Fig. 2.10, the cooling surface was circular and the impingement was done tangentially on the target wall. A lower aspect ratio showed an increase in the heat transfer for other conditions kept constant and an inclination of 60° was suggested to have minimum thermal stresses in the target surface.

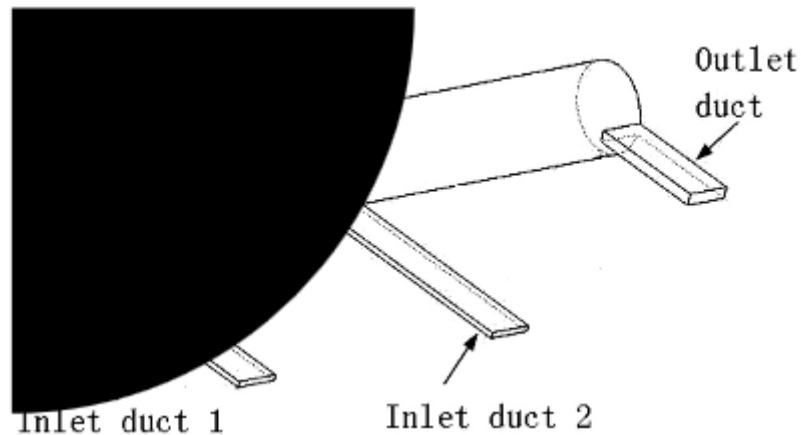


Fig 2.10 Tangential Flow as seen on the curved surface (Liu et al, 2015)

Flow from short hole channels of heights less than or equal to 1 jet diameter were conducted for discharging orthogonally into an open cross flow by Acharya et al. (Acharya et al, 2012). This was different from other jet impingement studies and more inclined towards film cooling which consists of covering the outer surface of the blade with the coolant. The goal here was to have the right amount of jet flow to effectively cool the blade without interfering with the hot gas momentum. The heat transfer was dependent on the blowing ratio (v_j/v_c) with the profile being more scattered for higher

blowing ratio with circulation due to the mixing of the cross flow and the jet causing impingement and flow separation on the target wall. This showed how an increase in the impingement favored parameter, G_c/G_j wasn't exactly helpful in using the same coolant properties for film cooling which may serve as an extension of jet impingement on the leading edge of the turbine blade.

Elebiary and Taslim (Elebiary et al, 2013) studied impingement on the leading edge of the turbine blade with exit from the same and opposite sides as the inlet and for a single inlet and two-way outlet. Four rows upstream were closed for a configuration, which were opened one-by-one for different setups in each case. There was a high dependency of Nu on the axial velocity of the upstream jets which caused the stagnation regions. Reversed flow was seen as expected due to the fountain effect of two adjacent wall jets. Hence, it was observed that two directional outlet was not any more efficient in removing heat for the given cases.

Most of the studies listed herein, showed the dependency of flow and geometric parameters on the cooling effectiveness of an impingement channel. To the knowledge of the author, no particular study highlighted on minimizing the coolant mass used for a given amount of cooling. In this study, the geometric parameters for an impingement channel (X/D and Y/D) are varied and tested for the same at a given Re .

3. Problem Statement and Objective

With high demand for increase in the performance capabilities of gas turbine engines, more work extraction is done by boosting the T_3 . With the temperature gap, between the material safe operating limit and turbine inlet temperature, of about 300°C (as listed before) and increasing (as seen in Fig. 3.1), it is imperative to ensure the higher amount of cooling demands be met. As the coolant air is bled directly from the compressor exit, it is imperative that minimum amount of coolant be used so that the trade-off (loss of air to increase T_3) proves to be beneficial.

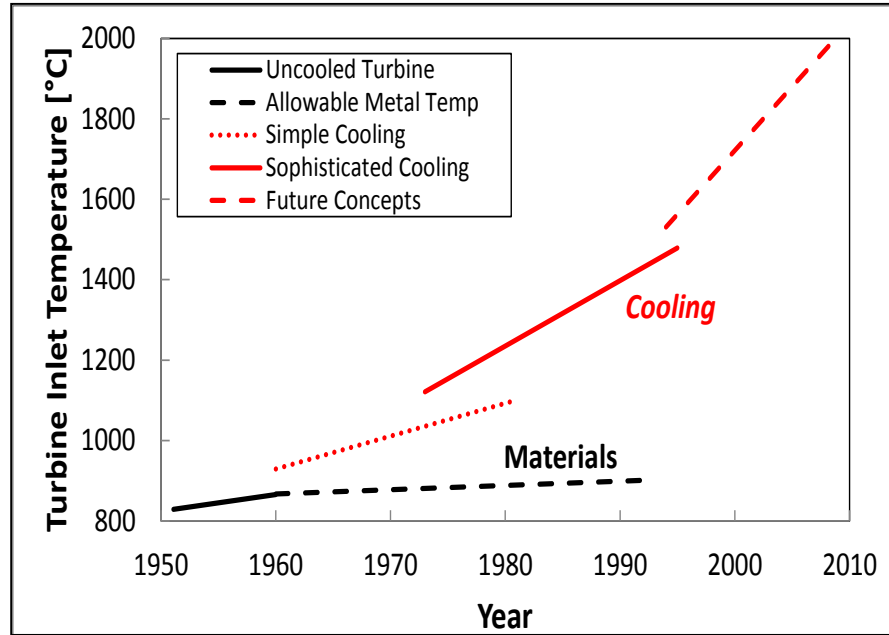


Fig 3.1 Increase in T_3 by material advances has been $4^\circ\text{C}/\text{year}$ approximately as compared to $11^\circ\text{C}/\text{year}$ by improvement in cooling technologies (Boyce, 2006).

Impingement channel cooling addresses this issue by internally cooling the blades for a given amount of coolant. As there is high turbulence seen in the engines, appropriate and adequate modeling of turbulence was of prime importance to understand the flow behavior, which is addressed in this study. The study also examines different

staggered and inline configurations of jet-to-jet spacing to reduce the amount of coolant required for the same amount of cooling attained by a baseline case which is an inline rectangular array of jets. For the same Re , comparisons are made in cooling performance to find the most effective configuration.

4. Methodology and Data Reduction

4.1 Experimental Model Setup

The setup was a scaled-up model of the inside of a turbine blade where a rectangular channel was used (Fig. 4.1a), 1.5 m long and 12 cm wide, made of acrylic $\frac{3}{4}$ " thick. It was closed from one end and connected to a blower with piping on the other end. This acted as a small portion of the curved internal surface, as seen in Fig. 4.1b, of the blade along the span.

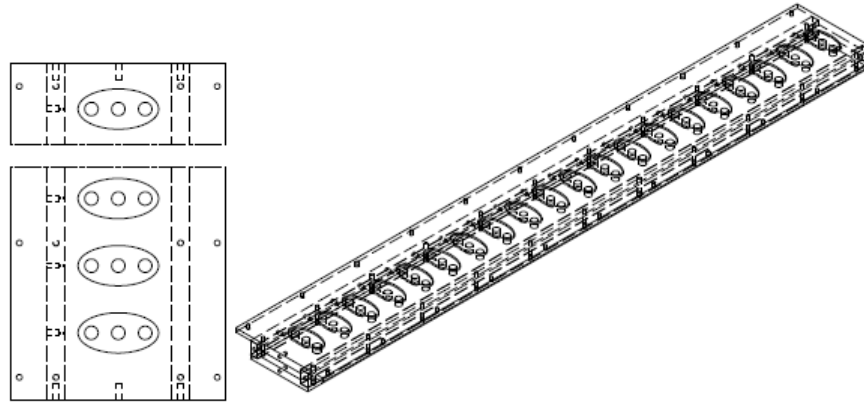


Fig 4.1a Geometry used for jet impingement

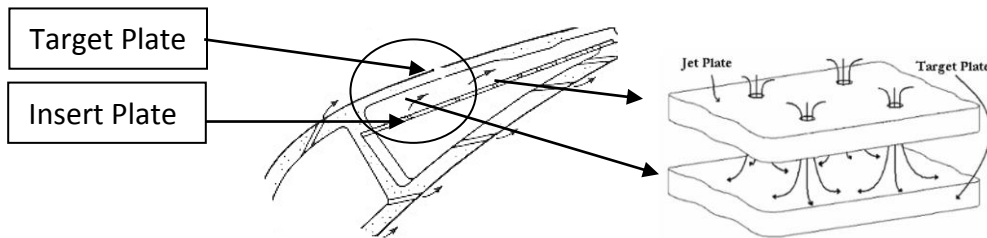
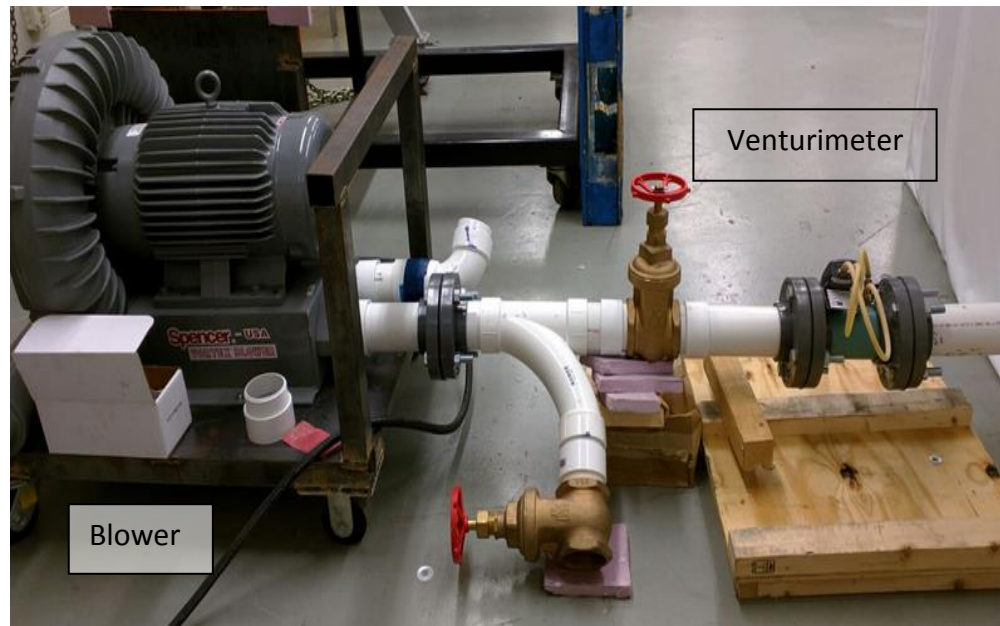


Fig 4.1b A small part of the blade surface representative of the channel used above (Herbert, 2004)

The blower provided constant mass flow which was measured by a venturi meter downstream as seen in Fig. 4.2. Gate valves were used to regulate the amount of mass

flow in the channel.



Gate Valves

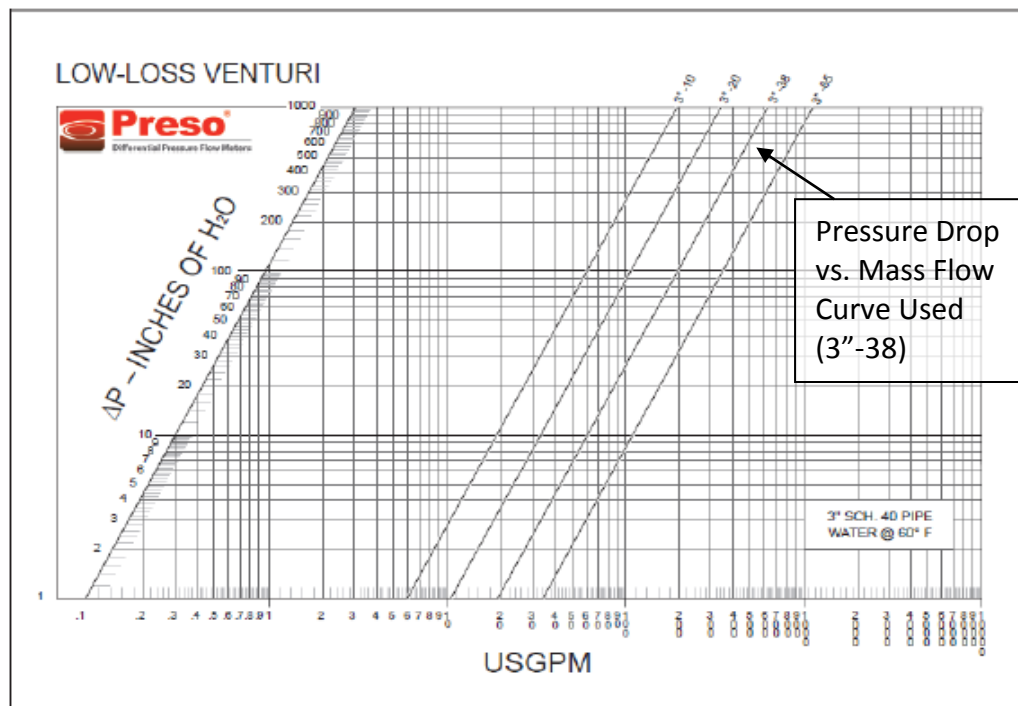


Fig 4.2 The blower with connected piping and gate valves to regulate mass flow in the channel (top). The mass flow was measured by measuring the pressure drop in the venture and calculating the appropriate relation for mass flow based on the pressure drop from the supplier provided chart (bottom).

A constant mass flow with a constant heat flux was used to replicate the engine conditions. The top plate of the channel acted as the insert plate and had a rectangular inline array of jets of diameter 15 mm. The bottom plate was the target wall on which the heater strips made of Inconel (Grade 625) were laid, as seen in Fig. 4.3.

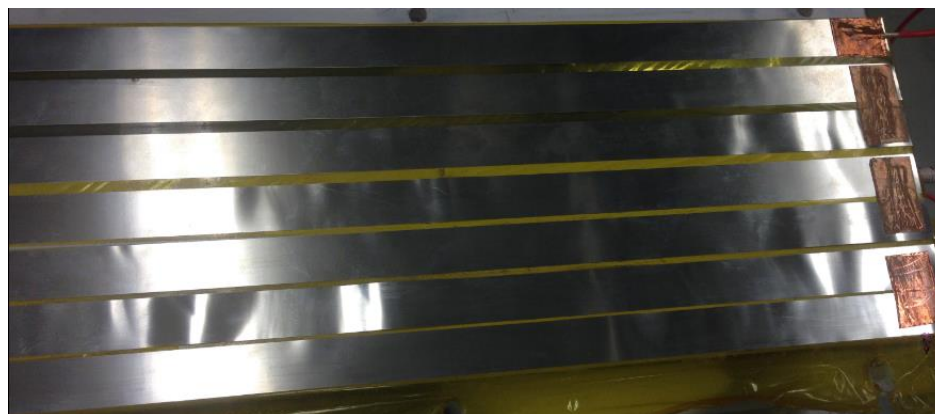


Fig 4.3 Inconel heater strips with copper bus bars connecting the ends.

Thermocouples were installed at the jet inlet and target wall to measure temperatures. They were heated by providing electrical current and Joule's law of heating was used to calculate the heat flux over the area of the strips. The target wall was painted with Temperature Sensitive Paint (TSP), which was first calibrated to get a temperature change for a known change in the intensity, as seen in Fig. 4.4. An intensity of ~ 450 nm was emitted using LEDs on the ISSI Unicoat UNT-12 TSP. The painted surface was heat treated to a maximum expected temperature. A higher intensity was seen as a result of cooler temperature as the vibrational energy of the molecules was converted to emission energy. With increasing temperature, more of the energy was converted to vibrational energy and less luminescence was seen, thus there was a lower intensity of the painted surface for a higher temperature (Liu, 2006).

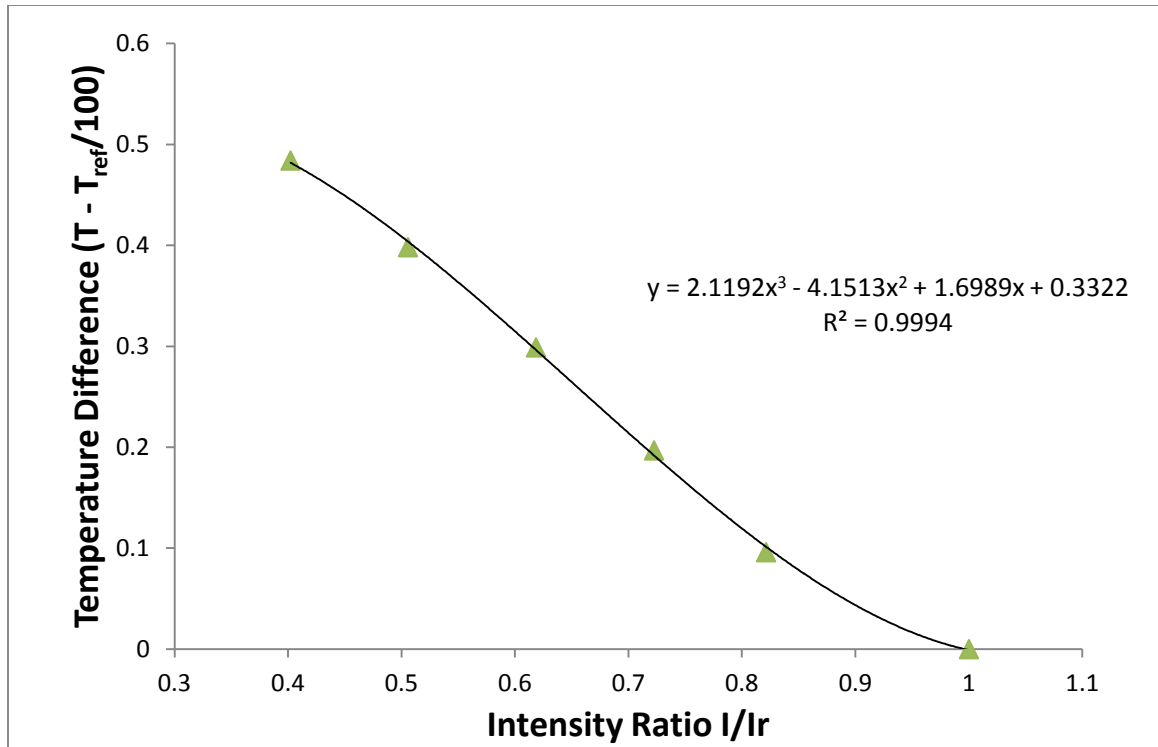


Fig 4.4 A typical calibration curve showing the temperature difference as a function of the intensity ratio (I/I_r)

This intensity ratio between a reference image (I_r) (image at a given temperature) and the data image (I) (hot image), as seen in Fig. 4.5a & b, was found by capturing the images using a charge coupled device (CCD) camera at a fixed exposure time. This was used to determine the temperature difference as shown above.

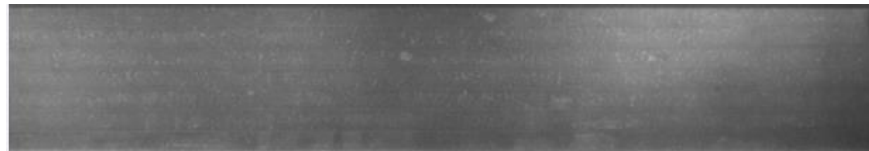


Fig 4.5a A sample of cold image of higher intensity



Fig 4.5b A sample of hot image of lower intensity

The temperature data acquired was used to find the Nu which was used to determine the cooling performance of a configuration for a given amount of mass flow in the channel. Two images were taken, using a traverse, as shown in Fig. 4.6, for the wall and they were stitched together to get the final results.

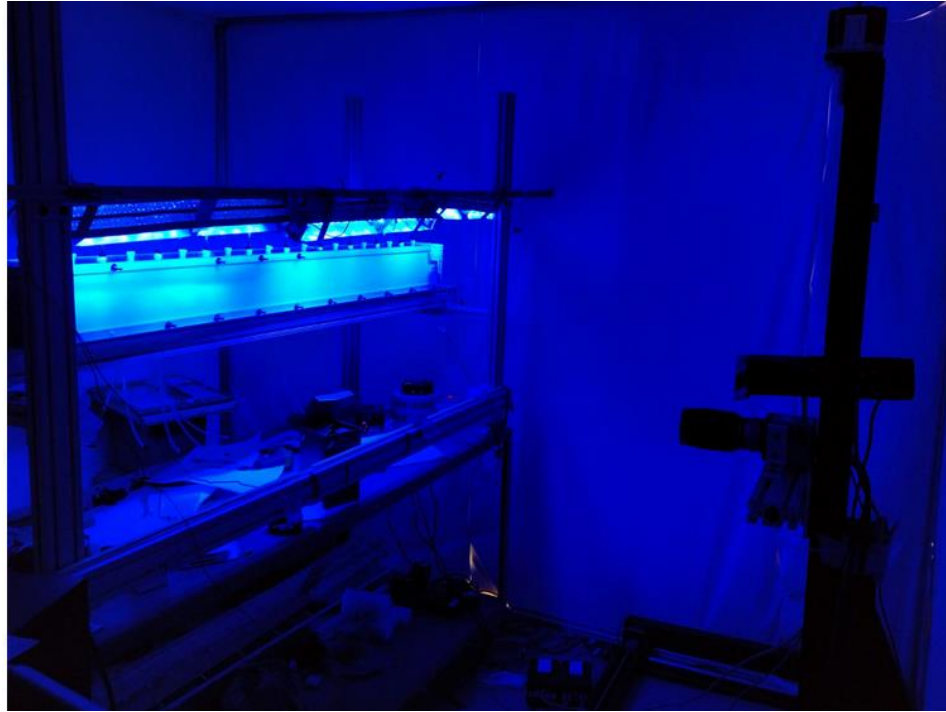


Fig 4.6 The set-up used with the traverse, LED lights and the CCD camera on the acrylic section

Pressure taps were installed along the length to obtain static pressures and mass flux profiles, G_c , G_j and $G_{j \text{ avg}}$. The following equation from isentropic relations was used to determine the mass flow rate from the pressure measured. The mass flow was then divided by the jet area to get the G_j and for a given X/D , the total mass flow through the upstream jets was divided by the channel area to get the G_c ,

$$m = C_d * [A_j * P_0 * \left\{ \left(\frac{P_s}{P_0} \right)^{\frac{\gamma+1}{2\gamma}} * \sqrt{\frac{2\gamma}{\gamma-1} * \frac{1}{RT_{avg}} * \left(\left(\frac{P_s}{P_0} \right)^{\frac{\gamma-1}{\gamma}} - 1 \right)} \right\}] \dots\dots\dots (9)$$

The Re was calculated from the mass flow as follows:

$$Re = m * d_j / (n * A_j) * \mu \quad \dots\dots\dots (10)$$

where the number of holes, n , were changed for different configurations.

Accounting for heat leakage was done by insulating the channel from the inside and applying a small amount of heat flux to check the change in surface temperature. This was related to the heat lost to the outside of the section and was used to calculate the heat flux loss to the surroundings at a given temperature difference.

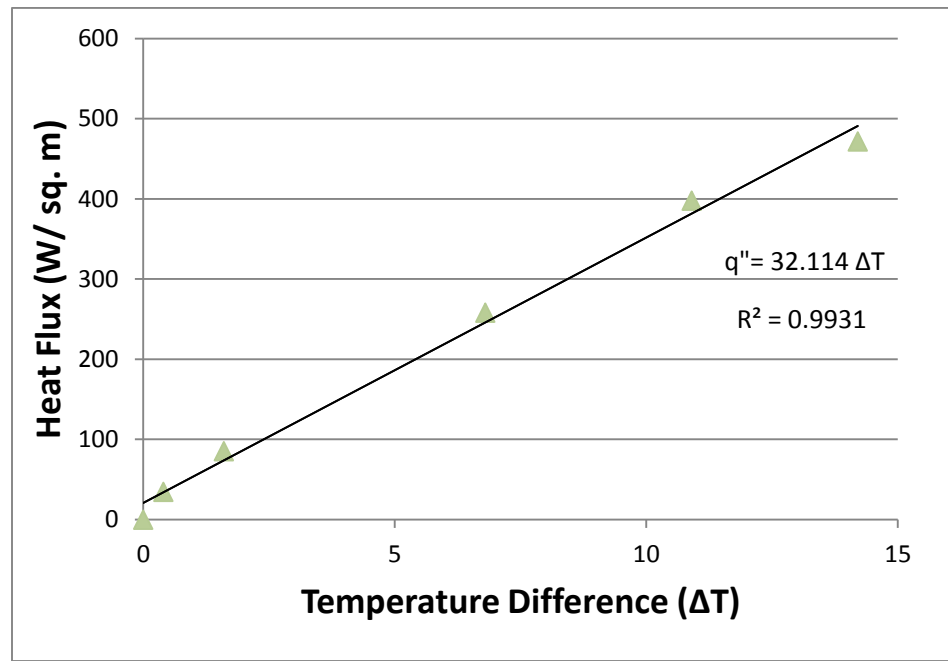


Fig 4.7 Heat Leak with increase in temperature

The heat flux in to the channel was denoted as follows, after accounting for the heat leaked:

$$q_{eff}'' = q''_{app} - q''_{leak} \quad \dots\dots\dots (11)$$

Based on the Newton's Law of Cooling, the following relation:

$$h = q'' / (T_w - T_j) \quad \dots\dots\dots (12)$$

where q'' was the heat flux generated, T_j being the jet (or coolant) temperature and T_w being the temperature of a point on the wall given by the TSP, the heat transfer co-efficient, h , and Nu based on the jet diameter were found.

$$Nu = hd_j / k_{air} \quad \dots\dots\dots (13)$$

An overall schematic of the full setup is shown here. The setup was checked for leakages and possible errors in connections. With the rig used under suction, air leaks were minimized and a tuft was used to check for leaks at points where there was doubt for the same.

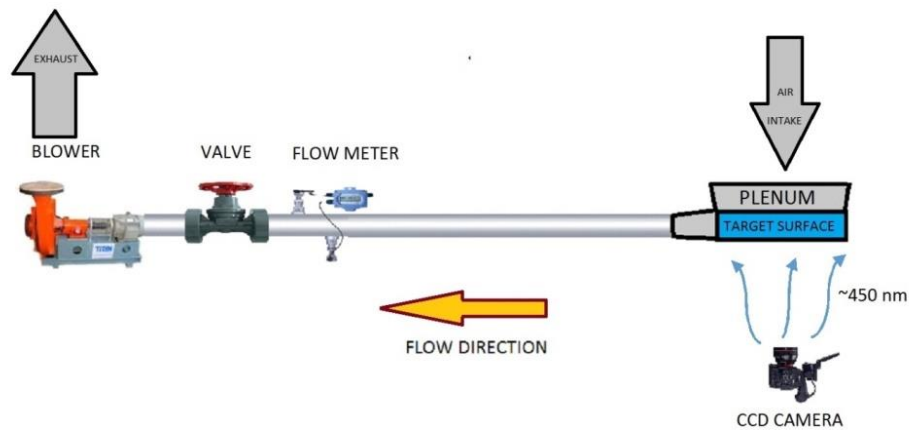


Fig 4.8 A schematic of the experimental setup used

4.2 Computational Model Setup

The computational model was set up for the air inside the channel. STAR-CCM+ was used to make the CAD geometry, create the mesh, simulate the model with the boundary conditions and post process. The mesh, as seen in Fig. 4.9a, was constructed using polyhedral elements and a surface wrapper with prism layers was added to capture

the normal temperature gradient and the boundary layer effects near the target wall. The prism layers used (Fig. 4.9b) was about 15% of the jet diameter and 20 layers were used with a growth rate of about 1.15. The wall y^+ values were of the order 10^{-3} signifying that the normal distance of the first cell centroid of the mesh was well within the viscous sub-layer.

The university supercomputer, RIGEL, was used to run the models with an average of 3 cores used in parallel computing per 1 million cells. The average time for convergence up to 5000 iterations was a little more than 24 hours, depending on cell count, as some cases needed an even higher cell count, in case convergence wasn't obtained. A UNIX based script was used to run the simulation files on the cluster. For STAR-CCM+ , a Java script was used where required to automate some of the iterative workflow for switching from one model to another or making minor changes in the mesh and geometry.

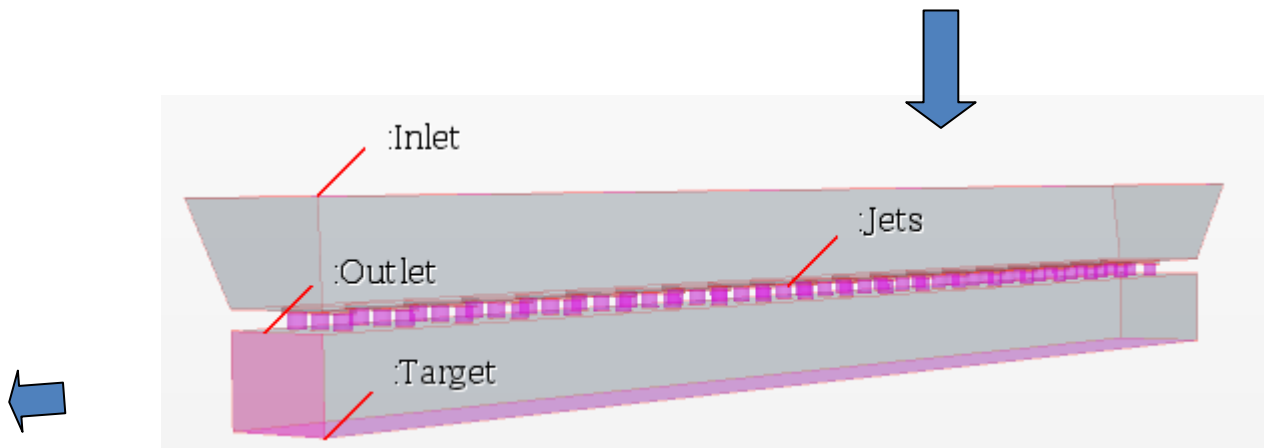


Fig 4.9a Geometry used for the simulation



Fig 4.9b Prism layers from the target wall of a total thickness of 15% of the jet diameter

5. Results and Discussion

5.1 Grid Independence Study and Channel Validation

A mesh independence study was conducted by running 5 different cell counts for the realizable k - ϵ model and the temperature on a node was found for all the cell counts. The boundaries were a mass flow inlet, a pressure outlet and a constant heat flux on the target wall while all the other surfaces were kept as walls. The boundary conditions were a heat flux of 1600 W/m^2 on the target wall, a mass flow inlet with the value adjusted for different Re and a zero gauge pressure at the outlet. The cell count of about 4 million gave an error of 0.1% compared to a count of 3 million, for the temperature on a node about 100 jet diameters downstream. But the turbulence model, v^2 - f , didn't converge for that mesh size and hence, the cell count was increased until a converged solution was obtained. This cell count was about 13.5 million and the parameter value varied by less than 0.1 % from the 3 million cell count. Hence, this model was selected for conducting further simulations.

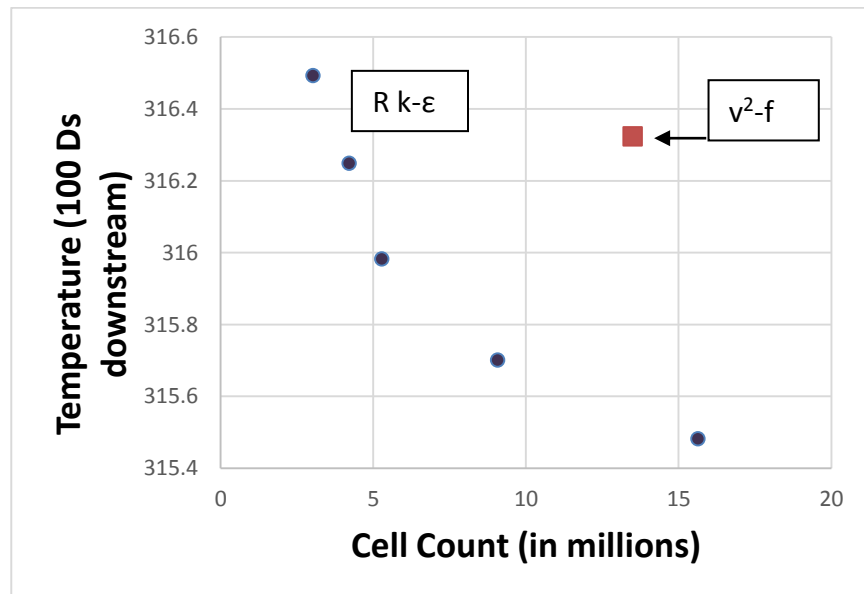


Fig 5.1 Temperature at a node plotted against cell count for Mesh Independence

For validating the smooth channel experiment with the existing correlations, the channel was opened from the upstream end with all the jet holes plugged and a constant heat flux was applied on the target wall. The reference and data images were taken for the TSP, based on which, the Nu was calculated. It was averaged into one value along the span, thus, resulting in a stream wise variation for a span wise averaged value.

The span wise averaged Nu was plotted and compared against Dittus-Boelter correlation. A Butterworth Filter was used to treat the values as a signal and smoothen the plot, as seen in Fig. 5.2.

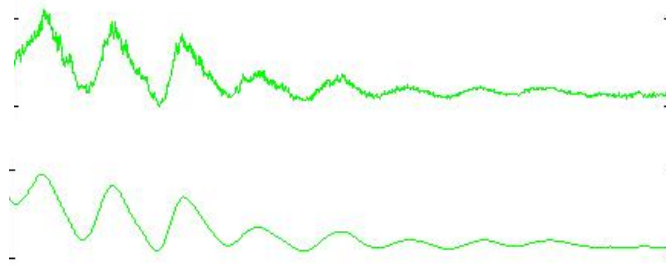


Fig 5.2 Sample Image before (top) and after (bottom) the Butterworth filter

The filter was set to a 4th order low pass type with a cutoff frequency between two adjacent points to be 0.02π rad/sec (MATLAB Online Documentation, 2015). For the given data set, this setting gave the least error (<2%) while preserving the trends.

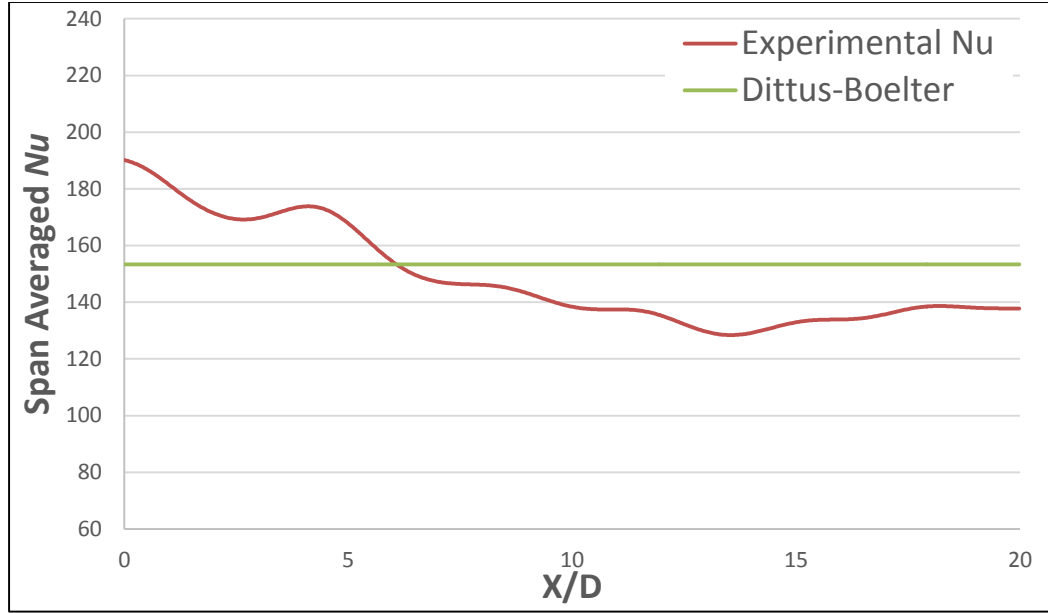


Fig 5.3 Span Averaged Nu for Experimental Rig

The matching of the experimental profiles within about 12% of the Dittus-Boelter correlation for heat transfer in a fully developed channel established the experimental setup as a valid model to replicate the internal flow in a channel and was used to model jet impingement.

5.2 Benchmarking of Turbulence Models

Different turbulence models were used to compare the heat transfer and flow results to the work done by Claret et al (Claret et al, 2011). Steady cases were run with different Reynolds Average Navier Stokes (RANS) models apart from the widely used $k-\epsilon$ and $k-\omega$ models. The EB $k-\epsilon$ and the v^2-f models were also used along with the realizable $k-\epsilon$ models with linear, quadratic and cubic constitutive relationship between stress and strain (STAR-CCM+ User Guide). This accounted for various terms such as the buoyancy, vorticity, rotation and anisotropy in the flow near the boundary layer and

areas of high wall normal turbulence. Better predictions of heat transfer in areas of high normal strain, as addressed before, were expected to be achieved by using the appropriate model.

The results for area averaged Nu were found from different models and were compared to the reference experimental data. The v^2 -f model gave the closest averaged value to the experimental data with an error of about 17.5% with EB k- ϵ being the second most accurate (~23%).

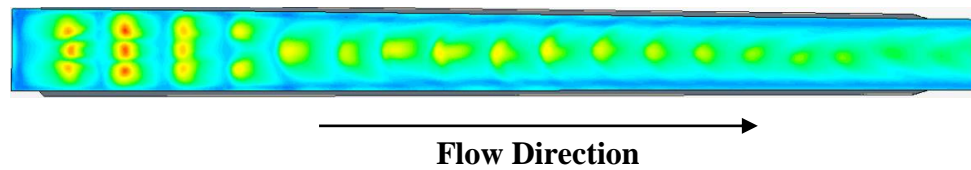


Fig 5.4 Contour Nu Plot on the target wall for v^2 -f turbulence model

As seen from Fig. 5.4, the stagnation peaks for the first three rows, are distinct for each jet. This number usually depends on the Re and Z/D as they determine the potential core of the jet impinging on the target wall. The transition to a single stagnation region is seen from the fifth row and some span wise deviation of the peaks from the centerline is seen even after averaging over iterations. The wetted area is also seen to reduce near the edges and beneath the fifth row is a visible bend of the same towards the downstream direction. This happens due to the dominance of the cross flow.

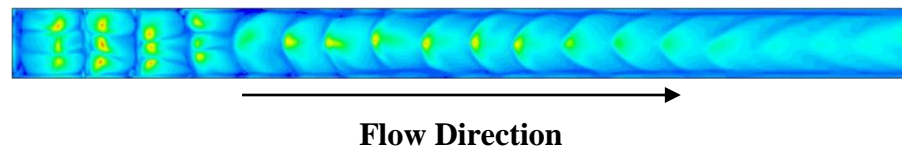


Fig 5.5 Contour Nu Plot on the target wall for EB k- ϵ turbulence model

The contour plot for the Nu was averaged over iterations. As this study assumes a steady case of the parameters, an average over iterations, makes it analogous to an

average over time.

Table 5.1 Surface averaged Nu values on the target wall for different models compared with the experimental data (Claretti et al, 2011)

Parameter	SST	EB	Quadratic (RKE)	Cubic (RKE)	V2-f	Exp.
Nu (Surf. Avg.)	50.51	53.47	41.42	41.31	57.08	69.15
% error	27.75	22.67	40	41.3	17.45	

Though, the experimental uncertainty in the reference data (Claretti et al, 2011) was about 12.3% for average Nu , without changing the model constants or in the mesh or solver settings, the above results were closer to predicting the stagnation point heat transfer than they were for the averaged heat transfer. A span wise averaged heat transfer plot confirms this assertion.

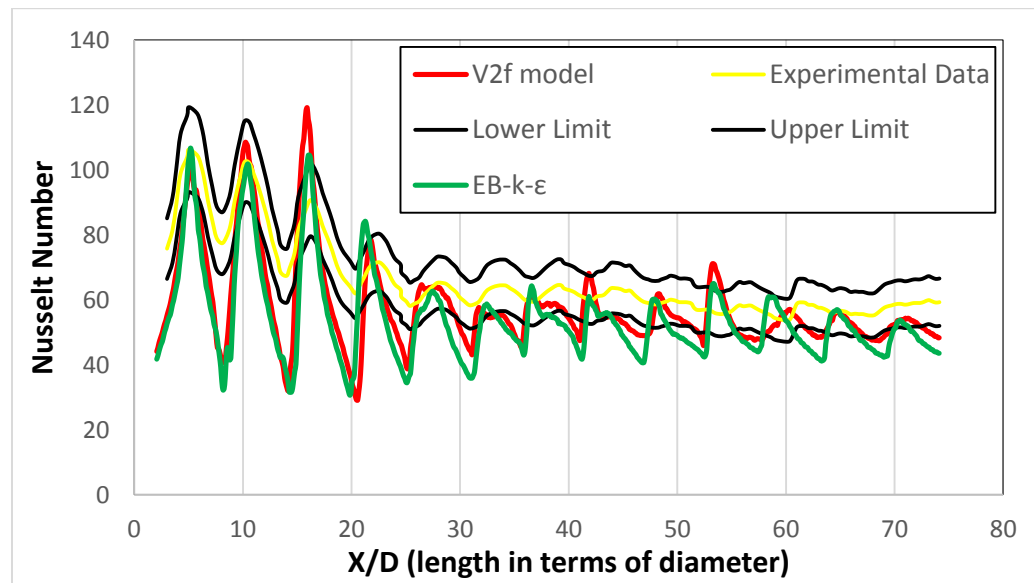


Fig 5.6 Span wise averaged Nu values on the target wall for different models compared with the experimental data (Claretti et al, 2011).

As can be seen from Fig. 5.6, both the v^2 -f and the EB k- ϵ models predicted the stagnation point heat transfers well within the range for the same Re as the experiment. In addition to this, there were a few anomalies seen in the span wise trends. The v^2 -f seemed to predict increasing stagnation point Nu for the first 3 rows with eventually to a steadily decreasing Nu and even further downstream, predicts a high stagnation point heat transfer than the rows upstream (for $X/D = 40 - 60$). While the EB k- ϵ predicts a steady Nu for the first 3 rows, it also makes similar predictions further downstream but for different X/D values. This is seen around the region where the $G_j/G_{j,avg}=1$ as seen in the plot below.

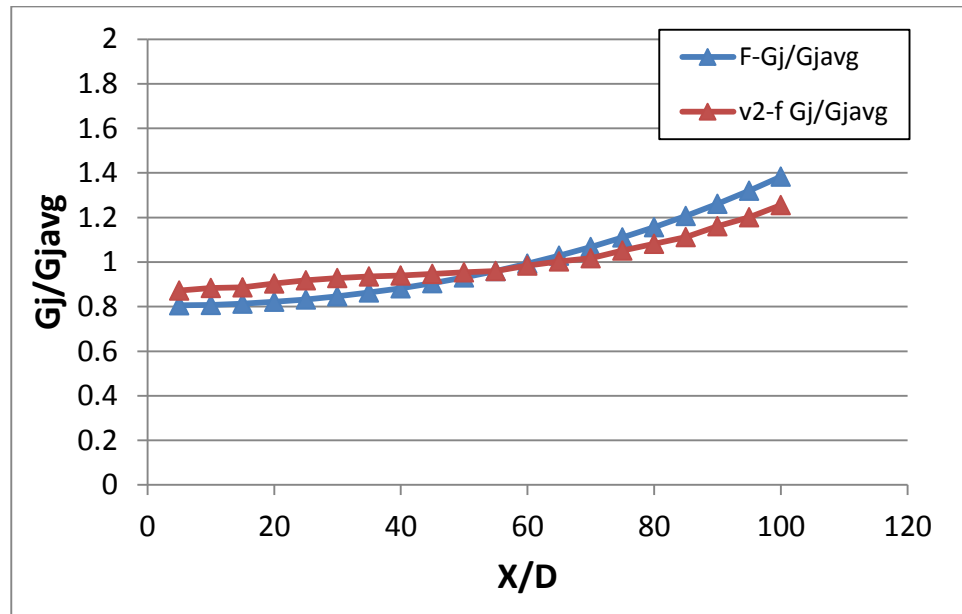


Fig 5.7 Jet mass flux to average jet mass flux ratios ($G_j/G_{j,avg}$) as obtained from the CFD model and compared with the analytical correlations (Florschuetz, 1981)

The maximum error was about 7% for the above plot which was under the 15% uncertainty of the correlation. There was interchanging accuracy between the predictions of EB k- ϵ and the v^2 -f model, but the latter needed a finer mesh to obtain a converged solution as compared to the EB k- ϵ for a relatively smaller change in accuracy. Also the

EB k- ϵ converged with less reversed flow and temperature (and/or pressure) corrections for a given mesh requiring lower computational time than the v^2 -f (20-25%).

A height wise effect of the impingement cooling on the target wall may be seen on a plane at different jet-to-plane distances. Illustrated in Fig. 5.8, are the results of the two different turbulence models in a height wise sense.

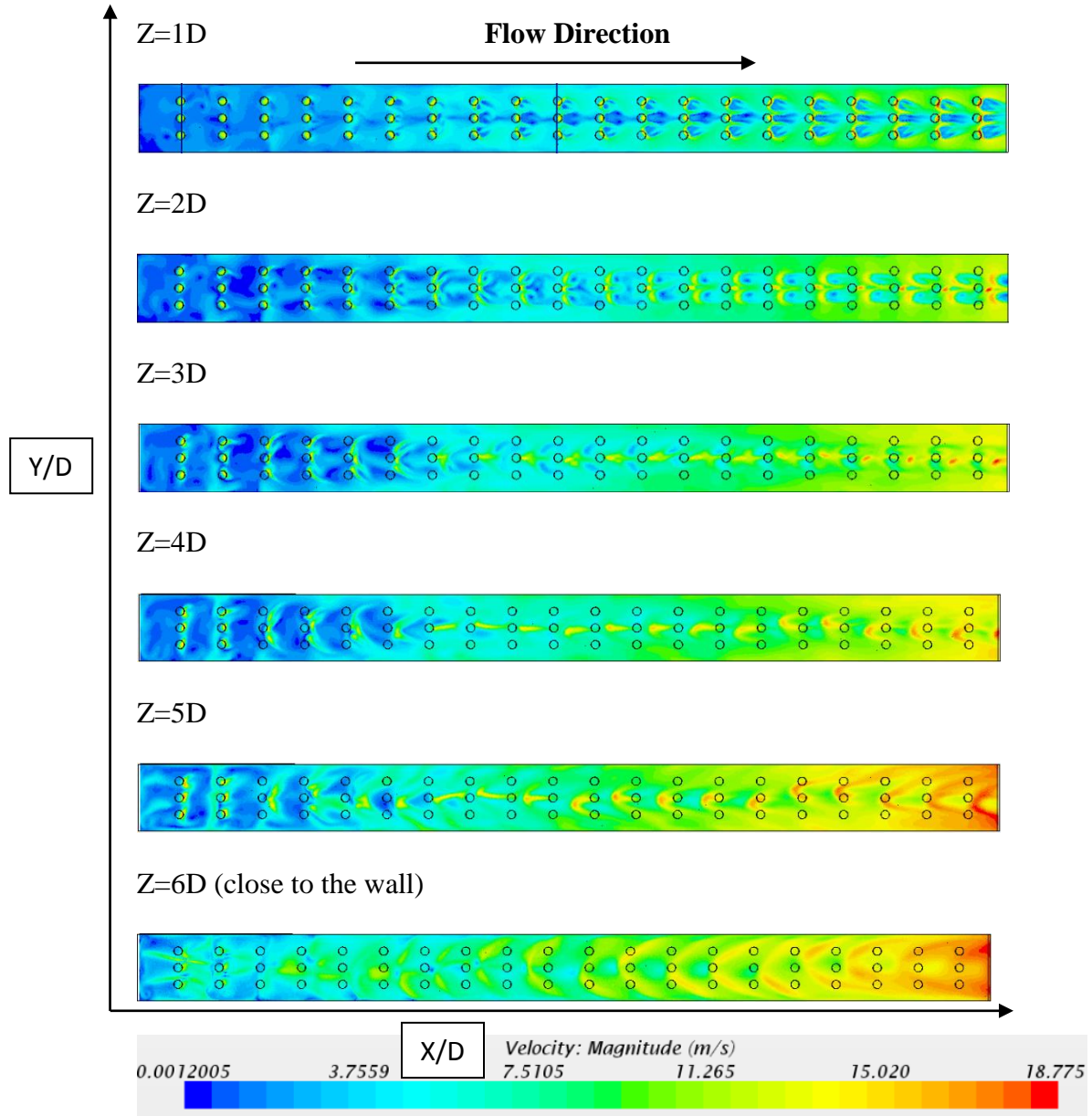


Fig 5.8 Spatial evolution of velocity contours along the channel height v^2 -f model

From the height 1D, it may be seen how the majority of the upstream cross-section has the higher velocity only right beneath the jets while from about the 13th row, is where the higher velocity is seen away from the jets. The jets are also seen deflecting towards the central jet for this row number which shows the rotation in the flow still has a dominating effect.

Between heights 2D and 3D, is where the contribution of the center jets seems to change its effect. The flow from the jets starts merging into one single stream along the center jet beginning from the 8th row. This effect is seen at the 4D height as well, but it is the 5D and 6D heights which show the spreading of the center jet in to two distinct streams near the 10th row. The cross flow breaks the combined jet effect discussed above, as seen on the 7th row, to a broken up profile resembling two angled lines, in a v-shape. The stagnation points being deflected from the jet location should also be noted.

A lower velocity is evident in the upstream region for the 1D height, but 2D onwards the wetted area increases and the amount of volume influenced by the jet also increases.

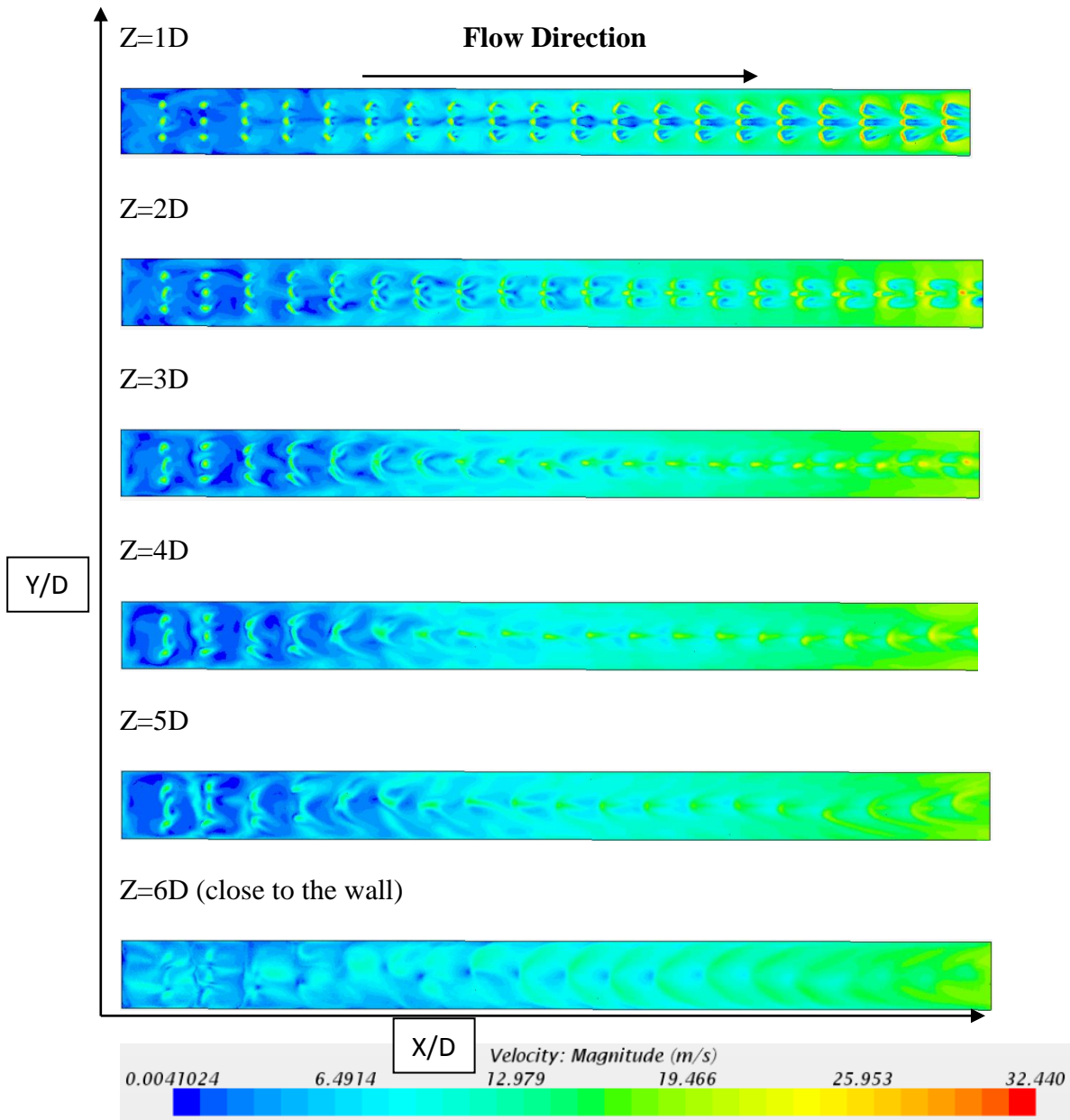


Fig 5.9 Spatial evolution of velocity contours along the channel height EB k- ϵ model

A similar breakdown for the EB k- ϵ model (Fig. 5.9) shows somewhat different trends. As is mentioned in the study by Manceau and Hanjelic (Manceau et al, 2002), the simplification of the Reynolds stresses in the model seems to have had an effect on the solution. There are trends similar to those observed for the v^2 -f, but the area of higher

momentum (velocity) which was clearly visible in the last few rows (in the green or yellow region), shows relatively lesser momentum for this model. The simplification of the six different Reynolds stresses in to one as carried out by this model, blended with the cross diffusion term appears to have had a more uniform distribution of the momentum. Even until the last 3-4 rows in the 5D height, the flow remains ‘unified’ contrary to what was seen for v^2 -f. Also seen is a lower effect of the cross-flow originating from upstream to the overall momentum downstream as the range of velocities observed and the area of the maxima seen are lower than their corresponding values for v^2 -f.

The heat transfer contour plots on the target wall were obtained and compared to those from the reference data, as seen in Fig. 5.10 (Claretti et al, 2011). After the 3rd or 4th row of jets, which corresponded to X/D of 15-20, the peaks predicted by the CFD appear shifted upstream as compared to the data. This relative shift from the experimental results was seen by El-Gabry (El-Gabry et al, 2005) and Claretti (Claretti et al, 2011) as well. The reason was believed to be the dominance of the cross-flow which resulted in moving the jet mass flux further downstream and also resulted in a stream wise elongation (at the outer jets) of the circular jet profiles seen for the first few rows upstream.

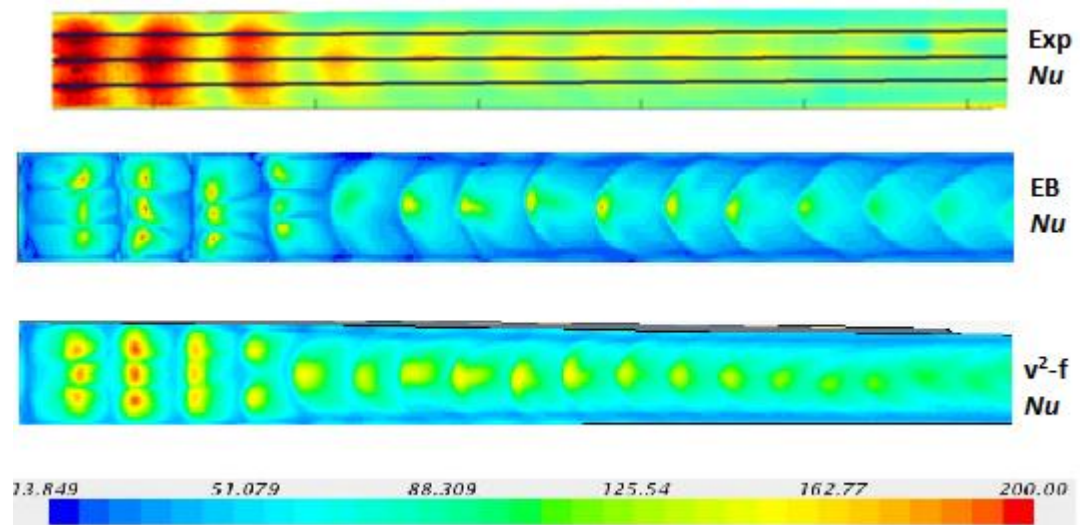
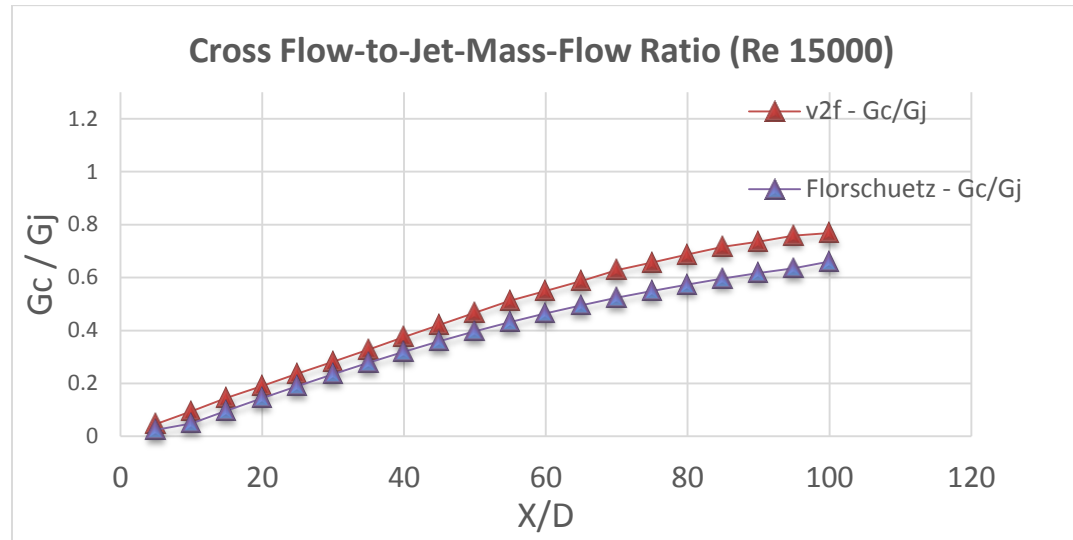


Fig 5.10 Target wall contours for Nu

The cross-flow mass flux to the jet mass flux profiles (G_c/G_j) which were believed to affect the heat transfer profiles further downstream were also compared with those from Florschuetz, as seen in Fig. 5.11 (Florschuetz et al, 1981). This was obtained with an error of around 14% which is within the model prediction range.

**Fig 5.11** Cross-flow to jet mass flux ratios (G_c/G_j) as obtained from the CFD model and compared with the analytical correlations (Florschuetz et al, 1981)

Different hole spacing configurations were chosen on preliminary CFD cases run for channel heights of 3D and 6D with two span wise spacing, 2D to 4D, and two stream wise spacing 5D and 10D. From the resulting 8 cases, it was observed that the area averaged Nu on the target wall was the highest for the spacing $X/D = 5$, $Y/D = 4$ for the height 3D.

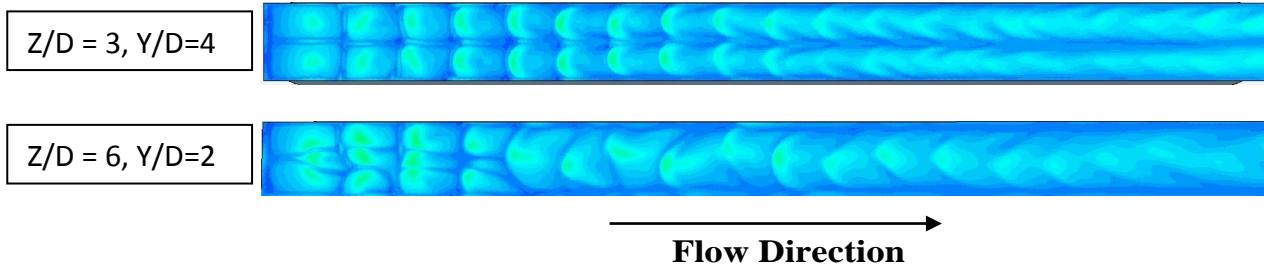
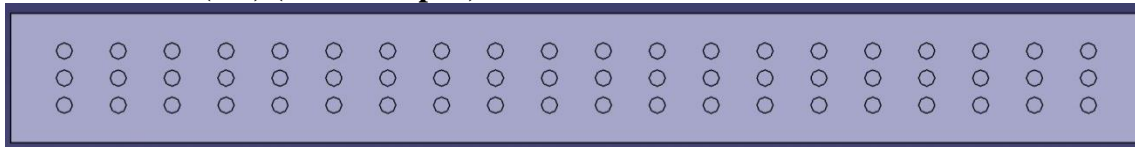
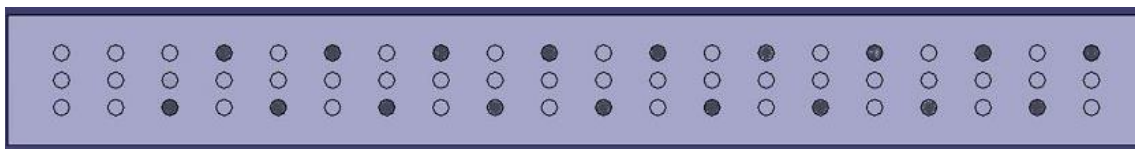
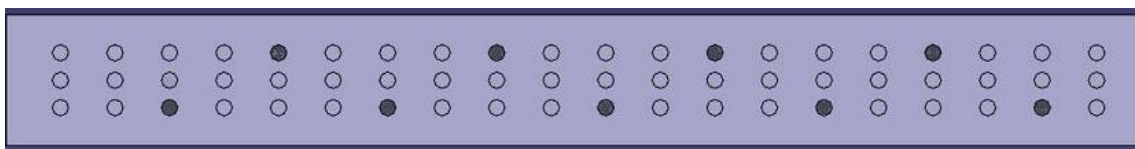
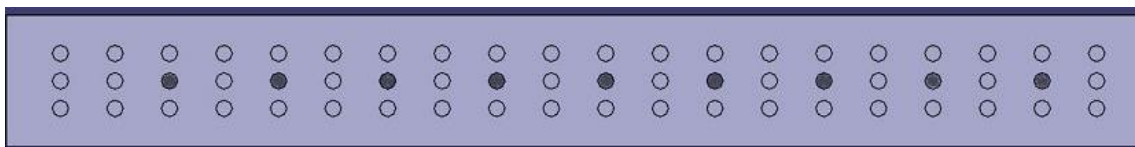


Fig 5.12 Nu contours on the target wall for 3D height with a 4D span wise spacing (top) and 6D height and 2D span wise spacing (bottom) as predicted from CFD using v^2 -f turbulence model.

It was also observed downstream, as in Fig. 5.12, that the stagnation region heat transfer circular profile was elongated and the number of stagnation regions, which should be equal to the number of rows were actually lesser as a result of the cross-flow blending.

Hence, the configurations were chosen such that there would be inline and staggered cases for a given Re and this apparent difference between the number of rows and the stagnation regions observed would decrease. A baseline configuration, as described above, was used as the reference to compare the performance of the configurations chosen. The filled holes were closed and the ones with only the outline shown were kept open, as may be seen in Fig. 5.13.

Baseline Case (BL) (all holes open)**Configuration A (Staggered, 18 holes closed)****Configuration B (Staggered, 9 holes closed)****Configuration C (Inline, 9 holes closed)****Configuration D (Inline, 18 holes closed)****Fig 5.13** Configurations chosen for different hole spacing

5.3 Experimental Results

Re: 20,000

The Nu contours were plotted from the image data processed in MATLAB by an in-house code. The baseline contours are compared with those from different configurations. A thermocouple was placed downstream, to get estimates of temperature on the wall to stay within limits of paint calibration, had a relatively higher impact on some of the images and is hence, omitted from consideration due to the same.

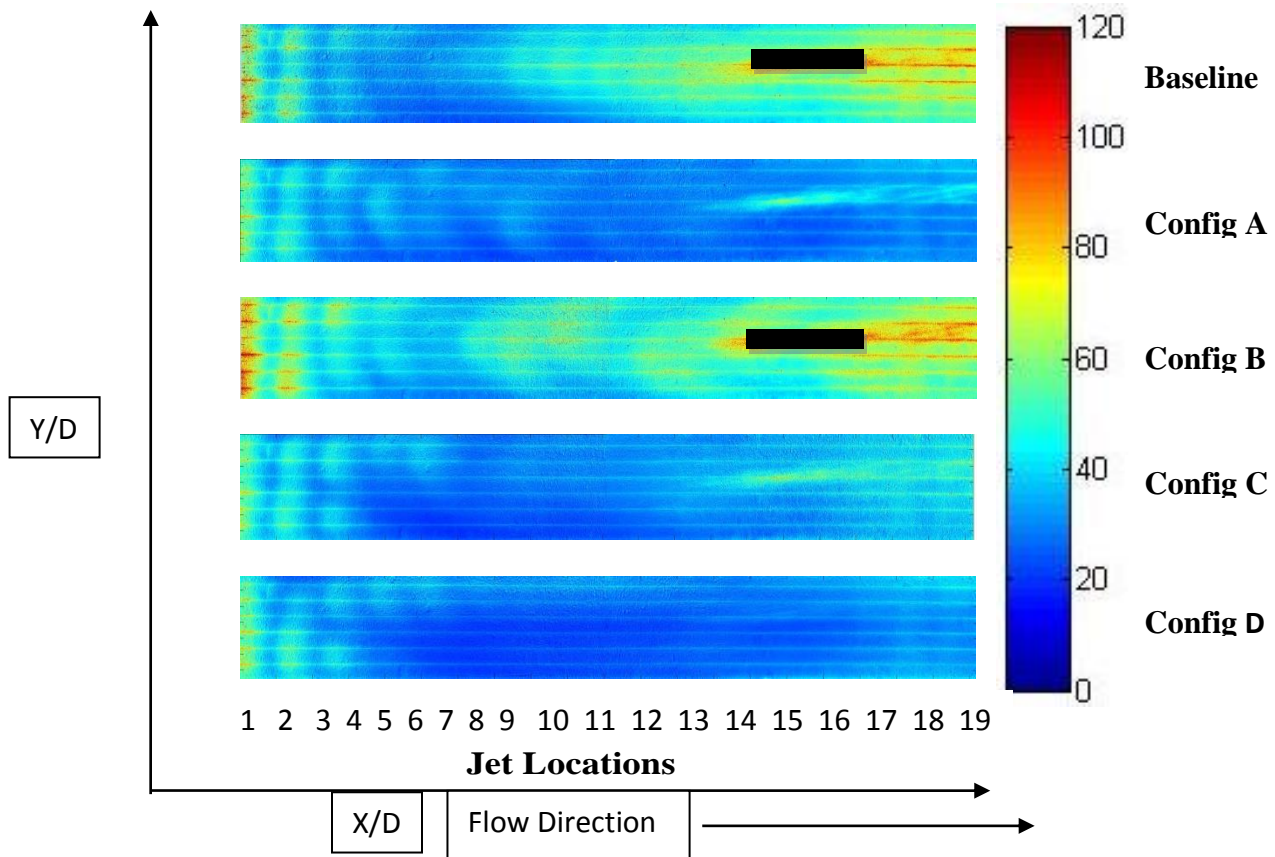


Fig 5.14 Nu Contours on the Target Walls

The stagnation points near the first 3 rows can be clearly seen in the Fig. 5.14, for all the cases. These regions see high localized cooling that is

characteristic of impingement profiles seen throughout the literature. For the baseline case, there is no clear maximum seen for the 4th row throughout the span, but from the 5th row onwards, the elongated profile is seen at the center. This is similar to that observed in the CFD profiles in the earlier images with a better averaged cooling and the cross-flow effects being dominant. This effect is seen throughout the rest of the channel with increasing wetted area as result of the cross-flow effected coolant.

For the configuration A, the 3rd and 4th maxima appear to show the effect of the hole being closed on one side of the span but on the 5th row, a better span wise cooling is observed. This seems as a result of the previous row wall jet affecting the jet flux downstream. This effect is seen until the 7th row with eventual disappearance of clear stagnation regions. This is the effect of the increasing cross-flow only showing an averaged cooling. The intensities of the maxima seen after the 4th row also drop, as is observed in the span averaged plots below.

For the configuration B the first two stagnation regions are also higher than the previous two cases resulting from higher momentum transport from the jet directly to the wall. With no stagnation points directly seen below the closed hole for the 4th row, as observed for the previous case, this configuration showed the elongated profiles. There were stagnation regions seen as predicted by CFD, for the baseline case, with some displacement from the center in both directions across the span.

Configurations C and D showed the initial stagnation points for the

first 3-4 rows, as seen in the cases before but the case C shows some signs of the average stagnation region along the center but the same cannot be said for case D. But, close observation leads to seeing that the periodic interference of the center jet in case C, gives a better average Nu after the 10th row, where $G_j/G_{j,avg} = 1$.

As the same amount of mass flow was required for the cases A and D and also for B and C, it may be concluded based on the above results, that the configuration B was more effective in removing heat for a given amount of coolant, with the highest heat transfer observed among the different configurations, but still about 20% lesser than that for the baseline.

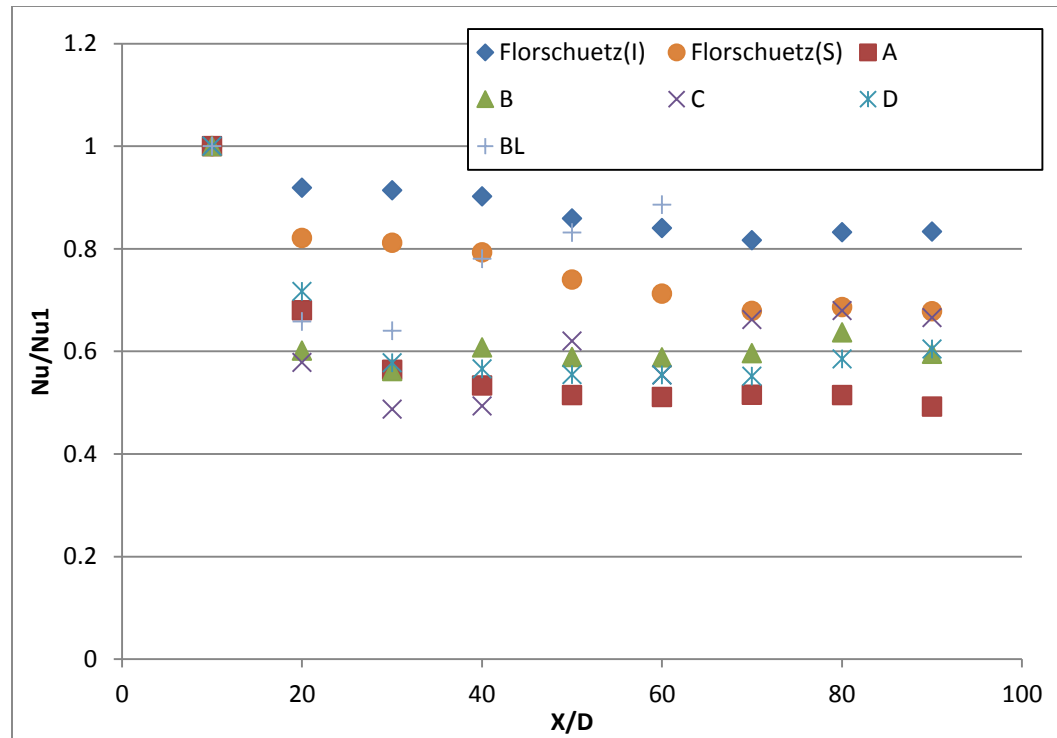


Fig 5.15 Span Wise Averaged Nu Plots

The span averaged plots at stagnation points were obtained, as in Fig. 5.15, between the Nu at a given location normalized by the Nu of the first

stagnation point. As the pressure was measured for every alternate row starting from the second row of jets, the corresponding value of Nu was used for normalizing the other stagnation points. Oddly, for the baseline case, the stagnation points at $X/D = 20$ and 30 plummet, compared to the correlation, and then fall back within the expected trends starting at $X/D=40$. This sudden drop may have been because of possible leaks left unchecked in the setup. For case B, the first stagnation region was relatively high and span averaged Nu appeared to increase after an X/D of about 30 , as predicted by the correlation (Florschuetz, 1981). It may be attributed to the increasing cross-flow which appears to have an initially negative effect, but becomes positive causing mixing and recirculation of zones with different temperatures. Also, seen is the convergence of the other cases towards a constant value, whereas, the cases B and C, show an increase.

But overall, the baseline case still stands strong on best average and local heat removal effectiveness with only the configuration B showing any promising results compared to other configurations, yet, having lower heat transfer.

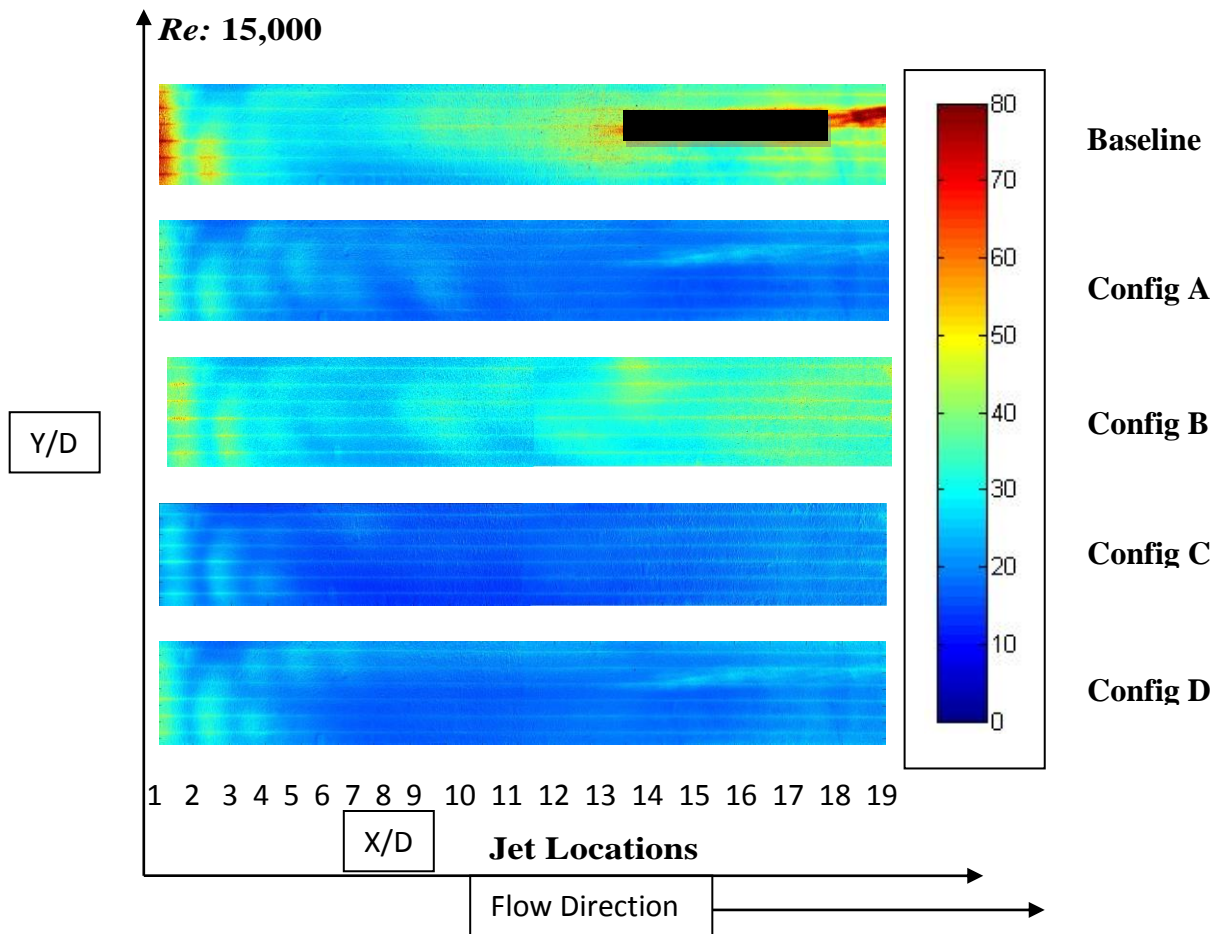


Fig 5.16 *Nu* Contours on the Target Walls

The *Nu* contours showed, in Fig. 5.16, similar trends for the lower *Re* with the baseline case showing the highest cooling effectiveness with the configuration B being the next best. The baseline contour showed a more uniform heat transfer after the first two rows itself and hence, a more uniform cooling than that observed for the higher *Re*. Whereas, the case B showed more pronounced stagnation regions for *X/D* of 35 to 55 before eventually blending and fading away of the profiles.

Although, for configurations A, C and D the average heat transfer is

not as high as for the other two cases, for this Re , the case D showed a better averaged cooling performance as compared to A or C. As A would be a more appropriate comparison to D (as they are staggered and inline cases of the same amount of mass flow) it may be observed that stagnation regions are seen until the 5th row for the case D and till the 7th row for A. But again, the marginal increase in the cooling effectiveness for D can be seen, which may be the result of the center jet having a higher effect on the momentum transfer to the wall compared to that of the cross-flow.

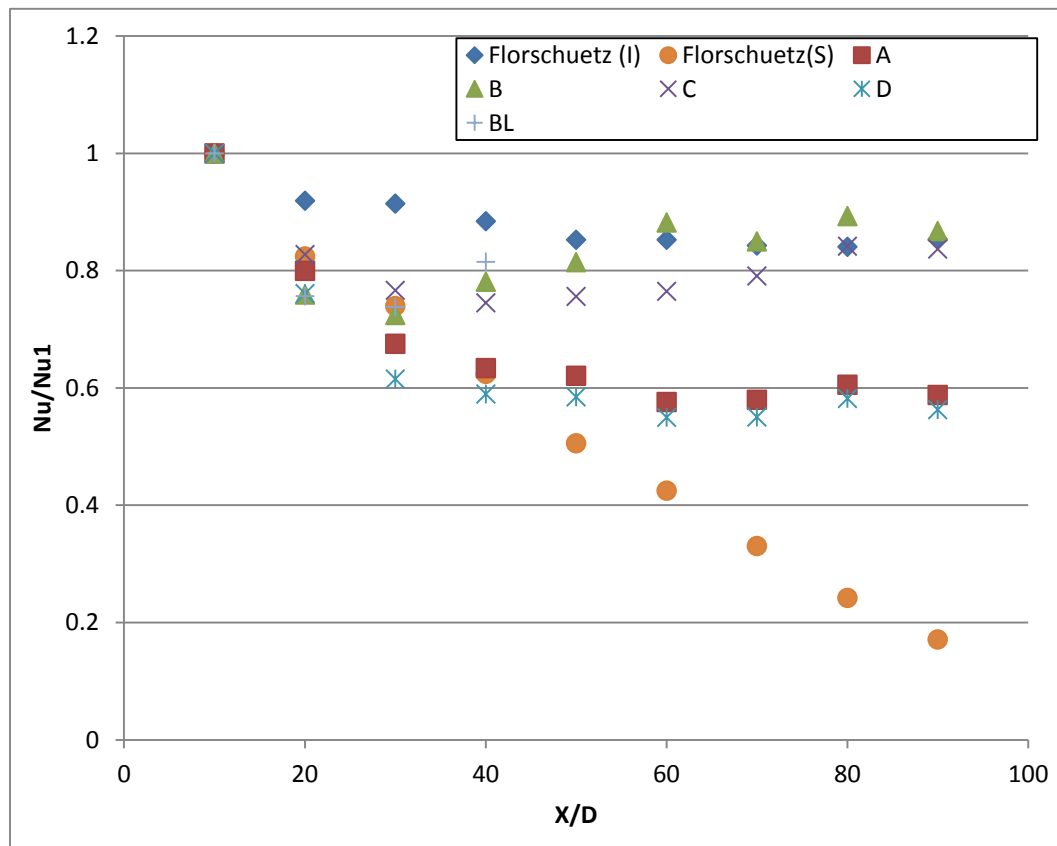


Fig 5.17 Span Averaged Nu plots at $Re=15000$

As may be seen from Fig. 5.17, configurations A and D fall well below the correlation predictions. Clearly, cases B and C have a better agreement with the

correlation and also have a somewhat increasing heat transfer with increase in distance along the stream. Configuration A sees a big drop from the first stagnation point until $X/D = 30$ before leveling out and eventually rising up towards the end. Configuration C also shows a steady increase in the heat transfer after $X/D = 40$, indicating some cross flow effects adding to the heat transfer. Also, a periodic contribution of the center jet appears to have caused an unexpected increase for both the Re . But as is clearly visible in the contour plots, the range of values displayed is lower by about 30% for the case C as compared to the baseline case. Hence, it was seen that the baseline case removes the maximum amount of heat for a given amount of mass of coolant. Though, the configuration B did show some promise, its overall or local effect was superseded by the baseline. A focus on the change in the profile expected and the factors causing it would better aid the purpose of this study in improving over the base line case.

6. Conclusions

1. Within the scope of this study, it was seen that the v^2 -f turbulence model, predicts the surface averaged Nu with the least amount of error, though there are some unexpected trends like increasing stagnation points for the first few rows or effect of wall jet on heat transfer peaks downstream. The flow conditions are predicted by both v^2 -f and the EB k- ϵ accurately to an extent. Though, the EB k- ϵ has smoother profiles, as a result of its simplicity, as compared to v^2 -f, the overall values predicted by it, were still a good bargain for the computing power it required.
2. Though, the extra accuracy of v^2 -f comes at the cost of high computing power, it gave about a 5-6% increase in accuracy for about 400% higher cell count than that required for all the other models. The EB k- ϵ predicted the trends with the next best accuracy with no cell refinement required or solver divergence issues. Given that experimental uncertainty is usually within the range of 8-9% for Re determination and about 12-14% for Nu (Ricklick, 2009), this appears to be a relatively smaller improvement for a significantly higher cost. Hence, where required, the EB k- ϵ can be used as an alternate to model jet impingement array cooling cases as the one investigated herein.
3. Among the different configurations used, it may be seen that the staggered configuration B exhibits relatively higher cooling effectiveness. But compared to the baseline configuration the values are still less by about 20-25%.

7. Scope for Future Work

The study conducted herein used an array of same sized holes. A possible improvement over this would be having different sized holes. Though, choking was observed in different sized holes as mentioned earlier (Florschuetz,1981), for an array of holes, the sizes in a given row may be varied to keep the jet mass flux ratio ($G_j/G_{j,avg}$) close to 1 throughout the span to have maximum jet momentum and hence, convective heat transfer throughout or locally.

As also observed previously, there is high turbulence in the potential core region, and the unsteadiness resulting from the same may be used to spread the jet cooling by changing the Re . An experimental study on the extent of the potential core in the jet axial direction, at different stream wise locations, could be conducted to give out an optimum height where the unsteady effects may be used to increase the stagnation area under the jet.

As the unsteady effects of the jets have been acknowledged in different studies, an experimental investigation with a time based temperature measurement technique, such as Transient Liquid Crystals (TLC), may be conducted to further understand the oscillations of the jet and different hole shapes may be used in the channel based on the patterns of the stagnation areas resulting from the jet shapes. For different stream wise spacing, along the channel, different hole shapes could be used to enhance heat transfer as compared to ribbed channels, which see a higher pressure drop and reversed flow, requiring more coolant mass.

REFERENCES

- Acharya, S. Eshtiaghi, A.H., Schilp, R. (2012) Flow distribution and heat transfer coefficients inside gas holes discharging into an orthogonal cross flow, *International Journal of Heat and Mass Transfer*, Vol. 55 pp. 7036-7045.
- Boyce M. P. (2006), *Gas Turbine Engineering Handbook*, 3rd Edition.
- Choi, M., Yang, G., Lee, J.S. (1998) An experimental study of slot jet impingement cooling on concave surface effects of nozzle configuration and curvature
- Claretti, R., Ricklick, M., Kapat, J. (2011) Computational and Experimental Comparison of Heat Transfer Characteristics of a Triple Row Impingement Channel at Different Heights.
- Cornaro, C., Fleischer, A.S., Goldstein, R.J. (1999) Flow visualization of a round jet impinging on cylindrical surfaces.
- Durbin, P.A. (1995) Separated Flow Computations with the $k-\epsilon-v^2$ Model, *AIAA Journal*, Vol. 33, No.4
- Efficiency of Ideal Brayton Cycle <http://image.frompo.com/b5b676831177714a8972be35cb3b8036>
- El-Gabry, L., Kaminski, D., (2005) Numerical Investigation of Jet Impingement with Cross Flow
- Elebiary K., Taslim, M.E. (2013) Experimental/Numerical Crossover Jet Impingement in an Airfoil Leading-Edge Cooling Channel, *Journal of Turbomachinery*, Vol.135, Issue 1.
- Florschuetz, L. W., Truman, C. R., Metzger, D. E., (1981) Streamwise Flow and Heat Transfer Distributions for Jet Array Impingement with Cross flow, *Journal of Heat Transfer*, Vol. 103, pp. 337.
- Gavrieli, K., Salim, N. Yanez, A. (2004) Jet Engine, A Historical Introduction <http://cs.stanford.edu/people/eroberts/courses/ww2/projects/jet-airplanes/how.html>
- Girardeau, J., Pailhes, J., Sebastian, P. Pardo, F., Nadeau, J., (2013) Turbine Blade Cooling System Optimization, *Journal of Turbomachinery*, Vol. 135, Issue 6
- Herbert, Ryan T. (2004), *Innovative Cooling Configurations for Low Emission Gas Turbine Combustors*
- Hallqvist, T., (2006) Large-eddy simulation of impinging jets with heat transfer, PhD Thesis, Royal Institute of Technology, Department of Mechanics, Sweden.

- Kanokjaruvijit, K., Martinez-botas, Ricardo F., (2004), Jet impingement on a dimpled surface with different cross flow schemes
- Liu, Quan (2006) Study of Heat Transfer Characteristics of Impinging Air Jet using Pressure and Temperature Sensitive Luminescent Paint.
- Liu Z., Li J.,Feng Z., Simon, T., (2015), Numerical study on the effect of jet nozzle aspect ratio and jet angle on swirl cooling in a model of a turbine blade leading edge cooling passage
- M. Behnia, S. Parneix, Y. Shabany, P.A. Durbin (1998) Numerical study of turbulent heat transfer in confined and unconfined impinging jets.
- Manceau, R., and Hanjelic, K. (2002) Elliptic blending model: A new near-wall Reynolds-stress turbulence closure
- Martin, H., (1977) Heat and Mass Transfer between Impinging Gas Jets and Solid Surfaces, Vol. 13
- MathWorks Documentation, MATLAB 2015b (2015) <http://www.mathworks.com/help/signal/ref/butter.html>
- Metzger, D. E., Florschuetz, L. W., Takeuchi, D. I., Behee, R. D., and Berry, R. A., (1979) Heat Transfer Characteristics for Inline and Staggered Arrays of Circular Jets With Crossflow of Spent Air, ASME J. Heat Transfer, 101 , pp. 526–531
- Mushatat. K.S.(2007) Analysis of the turbulent flow and heat transfer of the impingement cooling in a channel with cross flow, Journal of King Abdulaziz University, Vol. 18, No. 2, pp. 101-122, 2007.
- Net Generation (2015) by Energy source, Electric Power Monthly, June Edition, 2015, retrieved from: <http://www.eia.gov/electricity/monthly/pdf/epm.pdf>
- Park, J., Goodro, M., Ligrani, P., Fox, M., Moon, H. K. (2007) Separate effects of Mach Number and Reynolds Number on Jet Array Impingement Heat Transfer, Journal of Turbomachinery, Vol. 129, pp. 269-280, 2007
- Popiel, C.O., Trass, O. (1991) Visualization of a Free and Impinging Round Jet
- Ricklick, Mark A. (2009), Characterization of an Inline Impingement Channel for Turbine Blade Cooling Applications.
- Son, C., Gillespie, D., and Ireland, P. T., (2000) Heat Transfer and Flow Characteristics of an Engine Representative Impingement Cooling System, ASME Paper No. 2000-GT-219

- Tadhg S. O'Donovan, Fluid Flow and Heat Transfer of an Impinging Air Jet, University of Dublin, 2005
- Van Treuren, K. W., Wang, Z., Ireland, P. T., Jones, T. V., and Kohler, S. T. (1996) Comparison and Prediction of Local and Average Heat Transfer Coefficients Under an Array of Inline and Staggered Impinging Jet, ASME Paper No. 96-GT-163
- Wang, L., Sunden, B. (September, 2015). A novel control of jet impingement heat transfer in cross-flow by a vortex generator pair.
- Xing, Y., Spring, S., Weigand, B. (2010) Experimental and Numerical Investigation of Heat Transfer Characteristics of Inline and Staggered Arrays of Impinging Jets
- Yan, X., Sadei, N., (1997) Heat transfer from an obliquely impinging circular, air jet to a flat plate
- Zuckerman, N., Lior, N. (2006), Jet Impingement Heat Transfer: Physics, Correlations, and Numerical Modeling, Advances in Heat Transfer Vol. 39